Low-Dissipative High-Order Shock-Capturing Methods Using Characteristic-Based Filters[1]

H. C. Yee,* N. D. Sandham,† and M. J. Djomehri‡

NASA Ames Research Center, Moffett Field, California 94035; †Queen Mary and Westfield College, London, England; and ‡Calspan/NASA Ames Research Center, Moffett Field, California 94035

An approach which closely maintains the non-dissipative nature of classical fourth- or higher-order spatial differencing away from shock waves and steep gradient regions while being capable of accurately capturing discontinuities, steep gradient, and fine scale turbulent structures in a stable and efficient manner is described. The approach is a generalization of the method of Gustafsson and Olsson and the artificial compression method (ACM) switch of Harten. Spatially non-dissipative fourth- or higher-order compact and non-compact spatial differencings are used as the base schemes. Instead of applying a scalar filter as in Gustafsson and Olsson, an ACM switch is used to signal the appropriate amount of second- or third-order total variation diminishing (TVD) or essentially non-oscillatory (ENO) types of characteristic based numerical dissipation. This term acts as a characteristic filter to minimize numerical dissipation for the overall scheme. For time-accurate computations, time discretizations with low dissipation are used. Numerical experiments on 2-D vortical flows, vortex–shock interactions, and compressible spatially and temporally evolving mixing layers showed that the proposed schemes have the desired property with only a 10% increase in operations count over standard second-order TVD schemes. Aside from the ability to accurately capture shock–turbulence interaction flows, this approach is also capable of accurately preserving vortex convection. Higher accuracy is achieved with fewer grid points when compared to that of standard second-order TVD, positive, or ENO schemes.   © 1999 Academic Press

Key Words: low dissipation; high order; explicit and implicit finite difference methods; compact schemes; high-order central differencings shock-capturing methods; conservative differencing; shock–turbulence interaction; TVD schemes; positive schemes; ENO schemes.

1. INTRODUCTION

Modern shock-capturing methods such as total variation diminishing (TVD) or variants of essentially non-oscillatory (ENO) types of schemes that are higher than third-order accurate are usually CPU intensive, involve large grid stencils, and require special treatment near boundary points. In spite of their high-resolution shock-capturing capability, these schemes often exhibit undesirable amplitude and/or phase errors for vortical and turbulent convection flows and complex wave propagation phenomena. See NASA Conference Publication 3300, May 1995 [1], and Sandham and Yee [2] and references cited therein for some discussion. To compensate for the somewhat ad hoc ways of utilizing TVD, positive, or ENO schemes for compressible viscous flows, Toro [3] proposed a viscous flux limiter approach to deal with scalar mixed hyperbolic–parabolic problems. Systemic extension of Toro's idea to a system of equations containing other than a single scalar viscosity term remains a challenging area of research. The objective of this paper is to propose a compromise between the above two approaches while maintaining an efficient way to closely maintain fourth- or higher-order accuracy without using higher than third-order TVD or ENO dissipations. Hereafter we refer to "high-order schemes" as base schemes with spatial accuracy that is *greater than three*. The term base scheme will be defined in Section 2.

Accurate and efficient direct numerical simulation (DNS) of turbulence in the presence of shock waves represents a significant challenge for numerical methods. A numerical scheme for DNS of shock–turbulence interactions of high-speed compressible flows would ideally not be significantly more expensive than the standard fourth- or sixth-order compact or non-compact central differencing scheme. It should be possible to resolve all scales down to the order of the Kolmogorov scales of turbulence accurately and efficiently, while at the same time being able to capture steep gradients occurring at much smaller scales. Appropriate numerical schemes should not interfere with the turbulence mechanisms resulting directly from the governing equations. See Sandham and Yee [2] and references cited therein for a discussion.

Gustafsson and Olsson [4] developed stable high-order centered schemes with stable numerical boundary condition treatments. For problems containing shocks, they used a scalar shock-capturing filter. Such schemes have advantages over higher-order ENO schemes which require very large grid stencils even for modest orders of accuracy. (For example, a seven-point grid stencil is required for a second-order ENO scheme.) In this paper we propose to use the narrow grid stencil of high-order classical spatial differencing as base schemes. *Low-order TVD*, *weighted ENO* (*WENO*), *positive*, *and ENO dissipation* in conjunction with the Harten artificial compression method (ACM) switch [5] are used as characteristic filters. The ACM switch procedure is similar to Harten but applied in a slightly different context. The final grid stencil of these schemes, for example, is five if second- or third-order TVD or WENO schemes are used as filters and seven if second-order ENO schemes are used as filters for a fourth-order base scheme. Numerical boundary condition treatment is simple and can be the same as for the existing base and filter schemes. Here, we propose to use filter operators that have similar grid stencil widths as the base scheme for efficiency and ease of numerical boundary treatment. Higher than third-order filter operators are, of course, applicable, but they are more CPU intensive and require special treatment near boundary points for stability and accuracy. On the one hand, this would defeat the purpose of achieving efficiency. On the other hand, near shocks and shears, the resolution of higher-than-third-order TVD or ENO schemes is comparable to their lower-order cousin

except with a slight gain in resolution in regions near steep gradients and smooth flows. If lower-order filters are able to minimize but at the same time provide the proper amount of numerical dissipation away from shocks and shears to stabilize the non-dissipative nature of the high-order base scheme, we would achieve similar resolution with improved efficiency. This is the philosophy used to design the schemes. Our approach is aimed mainly at problems containing vortex convections, and shock, shear, and turbulence interactions. As illustrated in later sections, these types of characteristic TVD (and ENO or WENO) filters can even improve fine scale flow structure when applied to existing methods of Harten [6, 7] and Yee [8–10].

Section 2 describes the numerical algorithm. Section 3 illustrates the performance of these algorithms for a variety of unsteady flows where most conventional methods exhibit difficulty in obtaining low dissipative solutions in an efficient and stable manner. The first problem is a stationary vortex evolution. The second problem is a convecting vortex. In the third problem, a vortex pairing in a time-developing mixing layer, shock waves form around the vortices. In the fourth problem, a shock wave impinging on a spatially evolving mixing layer, the evolving vortices must pass through a shock wave, which in turn is deformed by the vortex passage. To demonstrate the applicability of these schemes in sustaining turbulence where shock waves are absent, a simulation of compressible turbulent channel flow in a small domain is carried out. For problems three and four, the detailed physics and extensive evaluation of the proposed scheme were reported in a separate paper by Sandham and Yee [2]. Here, only certain aspects of the performance of these schemes for the two problems are described. The study of the performance of this approach for time marching to the steady-state numerical solutions is in progress.

2. HIGH-ORDER SHOCK-CAPTURING SCHEMES USING CHARACTERISTIC FILTERS

For simplicity of presentation, the discussion will concentrate on the convection part of the Navier–Stokes equations. Analogous order of accuracy of spatial discretizations for the viscous terms will be briefly described at the end of this section.

In vector notation the 2-D compressible time-dependent Euler equations in conservation form for an equilibrium real gas can be written as

$$U_t + F_x + G_y = 0, \tag{2.1a}$$

where $U_t = \frac{\partial U}{\partial t}$, $F_x = \frac{\partial F}{\partial x}$, and $G_y = \frac{\partial G}{\partial y}$, and the U, F, G, vectors given by

$$U = \begin{bmatrix} \rho \\ \rho u \\ \rho v \\ e \end{bmatrix}; \quad F = \begin{bmatrix} \rho u \\ \rho u^2 + p \\ \rho u v \\ eu + pu \end{bmatrix}; \quad G = \begin{bmatrix} \rho v \\ \rho u v \\ \rho v^2 + p \\ ev + pv \end{bmatrix}. \tag{2.1b}$$

The dependent variable U is the vector of conservative variables, and $(\rho, u, v, p)^T$ is the vector of primitive variables. Here ρ is the density, u and v are the velocity components, ρu and ρv are the x- and y-components of the momentum per unit volume, p is the pressure, $e = \rho[\varepsilon + (u^2 + v^2)/2]$ is the total energy per unit volume, and ε is the specific internal energy.

For a thermally perfect gas, the equation of state is

$$p = \rho RT, \tag{2.2}$$

where R is the specific gas constant, and T is the temperature with $\varepsilon = \varepsilon(T)$. For constant specific heats (calorically perfect gas)

$$\varepsilon = c_v T, \tag{2.3}$$

where c_v is the specific heat at constant volume.

The eigenvalues associated with the flux Jacobian matrices of F and G are $(u, u, u \pm c)$ and $(v, v, v \pm c)$, where c is the sound speed. The two u, u and v, v characteristics are linearly degenerate. Hereafter, we refer to the fields associated with the $u \pm c$ and $v \pm c$ characteristics as the *nonlinear fields* and the fields associated with the u, u and v, v characteristics as the *linear fields*.

The basic idea of these shock-capturing schemes consists of *two steps*. The first step is the high-order spatial and temporal *base scheme*. Many standard high-order non-dissipative or low-dissipative base schemes fit in the present framework. The second step is the appropriate *filter* for stability, shocks, contact discontinuities, and fine scale flow structure capturing. Many TVD, positive, WENO and ENO dissipations, after a minor modification, are suitable candidates as filters.

2.1. The Base Schemes

In this paper, only the method of lines approach is considered. We divide the discussion of the base schemes into temporal and spatial base schemes. The filter step either does not directly involve the time discretizations or uses the same time discretizations as the base scheme, depending on the types of temporal schemes.

2.1.1. *Temporal Base Schemes*

Third- or higher-order linear multistep methods (LMMs) (Gear [11], Lambert [12]) are possible temporal base schemes. However they usually involve more than three time levels and initial starting schemes are required. For stiff problems, stiffly stable implicit methods as base schemes are desirable, especially for time marching to steady-state numerical solutions. Examples of explicit LMMs are explicit Euler and Adams–Bashforth. Examples of implicit LMMs are backward Euler, trapezoidal rule, and three-point backward differentiation. For non-stiff or moderately stiff multidimensional problems, one of the easiest procedures for obtaining higher than second-order temporal base schemes is the Runge–Kutta method. There are many variants of the Runge–Kutta method in the literature. See Lambert and Butcher [13], Carpenter and Kennedy [14], and Gottlieb and Shu [15] for details. Let

$$U_t = L(U)_{j,k} \tag{2.4}$$

be the semi-discrete form of (2.1), where L is the spatial discretization operator for $(-F_x - G_y)$ to be discussed in the next section. If viscous terms are present, L includes the viscous spatial discretizations. Here $U_{j,k}$ is a discrete approximation of U at $x = j\Delta x$ and $y = k\Delta y$, where Δx and Δy are the grid spacing in the x- and y-directions, and j and k are

the corresponding spatial indices. For simplicity of discussion, uniform Cartesian grids are assumed. Generalization of the method to nonuniform grids with analytical coordinate transformation is straightforward. For body conforming geometry without analytical coordinate transformation, the same spatial base scheme can be used to approximate transformation metrics.

The following indicate two possible explicit temporal base schemes. The fourth-order classical Runge–Kutta method takes the form

$$k_1 = L(U^n)$$
$$k_2 = L\left(U^n + \frac{\Delta t}{2}k_1\right)$$
$$k_3 = L\left(U^n + \frac{\Delta t}{2}k_2\right) \tag{2.5}$$
$$k_4 = L\left(U^n + \Delta t k_3\right)$$
$$\widehat{U}^{n+1} = U^n + \frac{\Delta t}{6}[k_1 + 2k_2 + 2k_3 + k_4].$$

Shu's third-order Runge–Kutta [16] form that is compatible with TVD, TVB (total variation bounded), and ENO schemes takes the form

$$U^{(1)} = U^n + \Delta t L(U^n)$$
$$U^{(2)} = \frac{3}{4}U^n + \frac{1}{4}U^{(1)} + \frac{1}{4}\Delta t L\left(U^{(1)}\right) \tag{2.6}$$
$$\widehat{U}^{n+1} = \frac{1}{3}U^n + \frac{2}{3}U^{(2)} + \frac{2}{3}\Delta t L\left(U^{(2)}\right).$$

Here $\widehat{U}^{n+1}$ might not be U^{n+1}—the full step Runge–Kutta solution at $n+1$—if the filter step is applied after the completion of the temporal base scheme. The procedure to apply the filter step will be discussed in Section 2.2.1.

In choosing an appropriate temporal base scheme, the order of the temporal discretization might not be the key measure of the choice of temporal method. At times, one may be mainly interested in the phase error of the solution. Schemes which have higher-order-accurate phase error might have lower order when measured in the standard L_2 norm. For hyperbolic and wavelike problems, one usually desires the accuracy in time and space to be equal. Another consideration is that the combined spatial and temporal discretizations might pose a very stringent time step constraint for the overall scheme. In addition, the proper choice of time discretization that is compatible with a chosen spatial discretization is crucial in achieving low phase and amplitude errors for time-accurate computations. This is a subject of ongoing research. For all the model test problems considered in this paper, the classical fourth-order Runge–Kutta method appears to work well.

2.1.2. *Spatial Base Schemes for the Convection Terms*

Denoting $F_{j,k}$ as the discrete approximation of the convection flux F at $(j\Delta x, k\Delta y)$, samples of the high-order base scheme for F_x (similarly for G_y) can be of the following four types.

Central differencings (fourth- and sixth-order).   Here

$$F_x \approx \frac{1}{12\Delta x}(F_{j+2,k} - 8F_{j+1,k} + 8F_{j-1,k} - F_{j-2,k}), \qquad (2.7)$$

$$F_x \approx \frac{1}{60\Delta x}(F_{j+3,k} - 9F_{j+2,k} + 45F_{j+1,k} - 45F_{j-1,k} + 9F_{j-2,k} - F_{j-3,k}). \qquad (2.8)$$

Compact central differencings (fourth- and sixth-order, Hirsh [17], Ciment and Leventhal [18], and Lele [19]).   Here

$$F_x \approx \frac{1}{\Delta x}\left(A_x^{-1} B_x F\right)_{j,k}, \qquad (2.9a)$$

where for a fourth-order approximation

$$(A_x F)_{j,k} = \frac{1}{6}(F_{j+1,k} + 4F_{j,k} + F_{j-1,k}), \qquad (2.9b)$$

$$(B_x F)_{j,k} = \frac{1}{2}(F_{j+1,k} - F_{j-1,k}), \qquad (2.9c)$$

and for a sixth-order approximation

$$(A_x F)_{j,k} = \frac{1}{5}(F_{j+1,k} + 3F_{j,k} + F_{j-1,k}), \qquad (2.9d)$$

$$(B_x F)_{j,k} = \frac{1}{60}(F_{j+2,k} + 28F_{j+1,k} - 28F_{j-1,k} - F_{j-2,k}). \qquad (2.9e)$$

Predictor–corrector differencings (fourth- and sixth-order).   Here

$$\text{Predictor:} \quad \frac{1}{6\Delta x}(-7F_{j,k} + 8F_{j-1,k} - F_{j-2,k}), \qquad (2.10a)$$

$$\text{Corrector:} \quad \frac{1}{6\Delta x}(7F_{j,k} - 8F_{j+1,k} + F_{j+2,k}), \qquad (2.10b)$$

and

$$\text{Predictor:} \quad \frac{1}{30\Delta x}(-37F_{j,k} + 45F_{j-1,k} - 9F_{j-2,k} + F_{j-3,k}), \qquad (2.11a)$$

$$\text{Corrector:} \quad \frac{1}{30\Delta x}(37F_{j,k} - 45F_{j+1,k} + 9F_{j+2,k} - F_{j+3,k}). \qquad (2.11b)$$

New forms of the upwind-biased predictor–corrector methods including compact formulations recently developed by Hixon and Turkel [20] are also applicable as spatial base schemes. Interested readers should refer to their paper for the various upwind-biased predictor–corrector formulae. The choice of the time integrators for these types of predictor–corrector methods is more limited. For example, if second-order time accuracy is desired, then (2.10) and (2.11) in conjunction with the *appropriate* second-order Runge–Kutta method are analogous to the familiar 2–4 and 2–6 MacCormack schemes developed by Gottlieb and Turkel [21] and Bayliss *et al.* [22]. Here the first number refers to the order of accuracy for the time discretization and the second number refers to the order of accuracy

for the spatial discretization. However, in this case one achieves the second-order time accuracy without dimensional splitting of the Strang type [23]. For higher-than-second-order time discretizations, only certain even stage Runge–Kutta methods are applicable. For compatible fourth-order Runge–Kutta time discretizations, see Hixon and Turkel for possible formulae. For example, the classical fourth-order Runge–Kutta is applicable provided one applies the predictor and the corrector step twice for the four stages, i.e., the predictor step for the first and third stages and the corrector step for the second and fourth stages.

The SHOEC differencings. The split high-order entropy conserving scheme (SHOEC) of Gerritsen [24] extends the summation by parts and entropy splitting idea of Olsson [25, 26] to the 2-D Euler equations for an ideal gas. It is based on the entropy splitting of the convection flux using Harten's symmetrized form via entropy variables [27]. Using the entropy variable transformation $W = W(U)$, one splits, for example,

$$F_x = \frac{\beta}{1+\beta} F_x + \frac{1}{1+\beta} F_W W_x \tag{2.12a}$$

with $\beta \neq -1$ and $F_W = \frac{\partial F}{\partial W}$. The vector W is chosen such that both $F(U(W))$ and $U(W)$ are homogeneous functions of the appropriate order β. For the perfect gas 2-D Euler equations W, and F_W and G_W are of the following form.

For $h(S) = K e^{S/(\alpha+\gamma)}$, where S is a dimensionless entropy (nondimensioned by C_v), K is a constant, and h is a differentiable function of S,

$$W = \frac{p^*}{p} \left[e + \frac{\alpha-1}{\gamma-1} p \quad -\rho u \quad -\rho v \quad \rho \right]^T, \tag{2.12b}$$

and the upper triangular part of the symmetric matrix U_W is

$$U_W = \frac{1}{p^*} \begin{bmatrix} a\rho & a\rho u & a\rho v & \frac{a}{2}\rho(u^2+v^2) - \frac{1}{\gamma-1}p \\ & a\rho u^2 - p & a\rho uv & u\left[\frac{a}{2}\rho(u^2+v^2) - bp\right] \\ & & a\rho v^2 - p & v\left[\frac{a}{2}\rho(u^2+v^2) - bp\right] \\ & & & -\frac{b}{\gamma-1}\frac{p^2}{\rho} - bp(u^2+v^2) + \frac{a}{4}\rho(u^2+v^2)^2 \end{bmatrix}. \tag{2.12c}$$

Here, p^* and p are related through

$$p^* = \chi e^{S/(\alpha+\gamma)} = \chi (p\rho^{-\gamma})^{1/(\alpha+\gamma)}, \tag{2.12d}$$

with $\chi = -\frac{K}{\beta}$. The variables p^* and β are given by

$$p^* = \frac{\gamma-1}{\alpha}\left(w_1 - \frac{1}{2}\frac{w_2^2}{w_3}\right), \tag{2.12e}$$

$$\beta = \frac{\alpha+\gamma}{1-\gamma}, \tag{2.12f}$$

where α is a constant. The constants a, b, and c are $a = (1-\alpha-\gamma)/\alpha$, $b = \gamma/(\gamma-1)$, and $c = (1-2\gamma)/(\gamma-1)$.

The flux vectors, expressed in the W variables, are given by

$$F(U(W)) = \frac{p}{p^*}\left[-w_2 \quad \frac{w_2^2}{w_4} + p^* \quad \frac{w_2 w_3}{w_4} \quad -\frac{w_2}{w_4}\left(w_1 + \frac{\gamma - \alpha}{\gamma - 1}p^*\right)\right]^T, \quad (2.12\text{g})$$

$$G(U(W)) = \frac{p}{p^*}\left[-w_3 \quad \frac{w_2 w_3}{w_4} \quad \frac{w_3^2}{w_4} + p^* \quad -\frac{w_3}{w_4}\left(w_1 + \frac{\gamma - \alpha}{\gamma - 1}p^*\right)\right]^T. \quad (2.12\text{h})$$

The upper triangular part of the symmetric matrices $F(U(W))_W$ and $G(U(W))_W$, expressed in the U variables, is given by

$$F_W = \frac{1}{p^*}$$

$$\times \begin{bmatrix} a\rho u & a\rho u^2 - p & a\rho uv & u\left[\frac{a}{2}\rho(u^2 + v^2) - bp\right] \\ & u(a\rho u^2 - 3p) & v(a\rho u^2 - p) & -b\frac{p^2}{\rho} + cpu^2 + \frac{a}{2}\rho(u^2+v^2)u^2 - \frac{1}{2}p(u^2+v^2) \\ & & u(a\rho v^2 - p) & uv\left[cp + \frac{a}{2}\rho(u^2+v^2)\right] \\ & & & u\left[bc\frac{p^2}{\rho} + cp(u^2+v^2) + \frac{a}{4}\rho(u^2+v^2)^2\right] \end{bmatrix},$$

$$(2.12\text{i})$$

$$G_W = \frac{1}{p^*}$$

$$\times \begin{bmatrix} a\rho v & a\rho uv & a\rho v^2 - p & v\left[\frac{a}{2}\rho(u^2 + v^2) - bp\right] \\ & v(a\rho u^2 - p) & u(a\rho v^2 - p) & uv\left[cp + \frac{a}{2}\rho(u^2+v^2)\right] \\ & & v(a\rho v^2 - 3p) & -b\frac{p^2}{\rho} + cpv^2 - \frac{1}{2}p(u^2+v^2) + \frac{a}{2}\rho(u^2+v^2)v^2 \\ & & & v\left[bc\frac{p^2}{\rho} + cp(u^2+v^2) + \frac{a}{4}\rho(u^2+v^2)^2\right] \end{bmatrix}.$$

$$(2.12\text{j})$$

In all of the numerical examples presented in Gerritsen [24], $\alpha = 1 - 2\gamma$.

The high-order base scheme using the SHOEC splitting applies the fourth- and sixth-order central differencings to F_x (and G_y) and W_x (and W_y). Note that this splitting of the flux consists of a conservative and a non-conservative part. The non-conservative part appears not to produce wrong shock locations traditionally associated with the use of non-conservative formulations of the Euler equation for computations. This splitting seems to require less numerical dissipation for the Euler computations over the non-split form. See Gerritsen [24] for illustration. Recently, Vinokur (1998, private communication) extended the SHOEC idea to a thermally perfect gas. Comparison of SHOEC with other base schemes requires a separate study and is in progress.

Stable boundary schemes for high-order base schemes. Consistent and stable one-sided boundary stencils for numerical boundary treatments using fourth- and sixth-order central spatial differencing have not been available until recently. These stable boundary schemes

employ the summation-by-parts idea to derive an energy estimate for the high-order central spatial differencings as interior schemes. See Kreiss and Scherer [28], Strand [29], and Gustafsson and Olsson [4] for the boundary scheme formulae.

2.1.3 Spatial Base Schemes for Viscous Terms

For simplicity let V_{xx} be a viscous term in one dimension. The possible high-order base schemes for V_{xx} can be as follows.

Central differencings (fourth- and sixth-order).   Here

$$V_{xx} \approx \frac{1}{12\Delta x^2}(V_{j+2} - 16V_{j+1} + 30V_j - 16V_{j-1} + V_{j-2}), \tag{2.13}$$

$$V_{xx} \approx \frac{1}{180\Delta x^2}(2V_{j+3} - 27V_{j+2} + 270V_{j+1} - 490V_j + 270V_{j-1}$$
$$- 27V_{j-2} + 2V_{j-3}). \tag{2.14}$$

Compact central differencings (fourth- and sixth-order, Hirsh [17], Ciment and Leventhal [18], and Lele [19]).   Here

$$V_{xx} \approx \frac{1}{\Delta x^2}\left(C_x^{-1} D_x V\right)_j, \tag{2.15a}$$

where for a fourth-order approximation

$$(C_x V)_j = \frac{1}{12}(V_{j+1} + 10V_j + V_{j-1}), \tag{2.15b}$$

$$(D_x V)_j = V_{j+1} - 2V_j + V_{j-1}, \tag{2.15c}$$

and for a sixth-order approximation

$$(C_x V)_j = V_{j+1} + a_0 V_j + V_{j-1}, \tag{2.15d}$$

$$(D_x V)_j = b_0(V_{j+1} - 2V_j + V_{j-1}) + \frac{c_0}{4}(V_{j+2} - 2V_j + V_{j-2}), \tag{2.15e}$$

$$a_0 = 5.5, \tag{2.15f}$$

$$b_0 = 4(a_0 - 1)/3, \tag{2.15g}$$

$$c_0 = (10 - a_0)/3. \tag{2.15h}$$

2.2. Characteristic Filters

In this section we first discuss the procedure for applying the characteristic filter for multistage and LMM types of time discretizations. We then discuss forms of the characteristic filter.

2.2.1 Procedure to Apply the Filter Step

If a multistage time discretization like the Runge–Kutta method is desired, the spatial base scheme discussed in the previous section is applied at every stage of the Runge–Kutta

method. If viscous terms are present, it is more consistent to use the same order and type of viscous base scheme as for the convection terms.

There are two methods in applying the characteristic filter. Method 1 is to apply the filter at every stage of the Runge–Kutta step. For inviscid and strong shock interactions, this approach might be more stable. The second method is to apply the filter at the end of the full Runge–Kutta step. Let $\widehat{U}^{n+1}$ be the solution after the completion of one full Runge–Kutta step of the base scheme advancement. Let L_f be the filter operator with

$$L_f(F^*, G^*)_{j,k} = \frac{1}{\Delta x}[\tilde{F}^*_{j+1/2,k} - \tilde{F}^*_{j-1/2,k}] + \frac{1}{\Delta y}[\tilde{G}^*_{j,k+1/2} - \tilde{G}^*_{j,k-1/2}], \quad (2.16)$$

where $\tilde{F}^*_{j+1/2,k}$ and $\tilde{G}^*_{j,k+1/2}$ are the dissipative numerical fluxes for the filter operator. Hereafter, we refer to $\tilde{F}^*_{j+1/2,k}$ and $\tilde{G}^*_{j,k+1/2}$ as the "filter numerical fluxes." Possible formulae for the filter numerical flux will be discussed shortly. Then, we define the new time level as

$$U^{n+1} = \widehat{U}^{n+1} + \Delta t L_f(F^*, G^*)_{j,k}. \quad (2.17)$$

The filter numerical fluxes $\tilde{F}^*_{j+1/2,k}$ and $\tilde{G}^*_{j,k+1/2}$ are evaluated at $\widehat{U}^{n+1}$. If physical viscosity is present, method 2 can be viewed as a mechanism in applying the filter with the physical dissipation taken into consideration. In all of the numerical examples, method 2 is used.

If one desires a time discretization that belongs to the class of LMMs, then the filter operator L_f can be applied as a dissipative numerical flux in conjunction with the base scheme. The filter numerical flux $\tilde{F}^*_{j+1/2,k}$ and $\tilde{G}^*_{j,k+1/2}$ in this case are evaluated at U^n for explicit LMMs. For implicit LMMs additional similar filter numerical fluxes evaluated at the $n + 1$ time level are involved. Alternatively, procedure (2.17) can be applied to LMMs as well, where $\widehat{U}^{n+1}$ is the solution after the completion of one LMMs step of the base scheme.

For time marching to steady states using implicit LMMs, certain flow physics only requires an explicit dissipation term. Also, the implicit operator can be different from the explicit operator. See Yee [8, 30, 31] and Yee *et al.* [32] for some efficient conservative linearized implicit forms.

2.2.2. *The Filter Numerical Fluxes*

There are many possible candidates for the filter operator in conjunction with high-order base schemes. Here, we propose to use filter operators that have similar width of grid stencils as the base scheme for efficiency and ease of numerical boundary treatment. Higher-than-third-order filter operators are, of course, applicable, but they are more CPU intensive and require special treatment near boundary points for stability and accuracy. On the one hand, this would defeat the purpose of achieving efficiency. On the other hand, near shocks and shears, the resolution of higher-than-third-order TVD, WENO, or ENO schemes is comparable to that of their lower-order cousin except with a slight gain in resolution in regions near steep gradients and smooth flows (Engquist and Sjogreen [33], Donat [34], and Carpenter and Casper [35]). If the lower-order filters are able to minimize but at the same time provide the proper amount of numerical dissipation away from shocks and shears to stabilize the non-dissipative nature of the high-order base scheme, we would achieve similar resolution with improved efficiency. This is the philosophy used to choose the filter numerical fluxes.

The simplest form is a scalar linear filter proposed by Gustafsson and Olsson [4]. It is a similar form used by Jameson *et al.* [36] to supply a linear second-order dissipation to a low-order (second-order) central differencing for shock-capturing purposes. Gustafsson and Olsson used a switch similar to that of Harten [5]. The Harten switch was designed for self-adjusting hybrid schemes between Harten's first-order ACM scheme and second- or higher-order schemes. Instead of switching from a higher-order scheme to a first-order scheme for shock and shear capturing, we generalized Harten's idea of achieving, in a loose sense, a low-dissipative high-order shock-capturing scheme by nearly maintaining the accuracy of the high-order non-dissipative property using nonlinear characteristics-based filters. The reason for the nonlinear characteristic base filters is that scalar linear filters do not take into account the different wave characteristics of the Euler equations. For complex shock waves and shear–turbulence interactions, one has better control of the amount of dissipation associated with each wave.

Filter numerical fluxes and nonlinear dissipation of shock-capturing schemes. We start with any second- or third-order TVD, positive, WENO, or ENO scheme that can be *recast* as the sum of *central differencing* and *nonlinear dissipation terms*. Recall that the Harten [6, 7], Yee and Harten [37], and Yee's [8] symmetric TVD schemes are already cast in this form. For example, let L_{tvd} be a TVD (or ENO) spatial operator with

$$L_{\text{tvd}}(F, G)_{j,k} = \frac{1}{\Delta x}[\tilde{F}_{j+1/2,k} - \tilde{F}_{j-1/2,k}] + \frac{1}{\Delta y}[\tilde{G}_{j,k+1/2} - \tilde{G}_{j,k-1/2}]. \quad (2.18)$$

Take, for example, the F flux. We cast the numerical flux $\tilde{F}_{j+1/2,k}$ into the form

$$\tilde{F}_{j+1/2,k} = \frac{1}{2}[F_{j+1,k} + F_{j,k} + R_{j+1/2}\Phi_{j+1/2}]. \quad (2.19)$$

Here, $\frac{1}{2}[F_{j+1,k} + F_{j,k}]$ is the central differencing portion of the numerical flux $\tilde{F}_{j+1/2,k}$, and the last term $R_{j+1/2}\Phi_{j+1/2}$ (with the suppression of the k index) is the "nonlinear dissipation." For characteristics-based methods, the quantity $R_{j+1/2}$ is the right eigenvector matrix of $\frac{\partial F}{\partial U}$ using, for example, Roe's approximate average state. Note that the eigenvector $R_{j+1/2}$ should not be confused with the R in (2.2). Similarly, we cast the $\tilde{G}_{j,k+1/2}$ in the same manner.

We use these nonlinear dissipation terms in conjunction with Harten's switch applied to each characteristic wave as the filter numerical fluxes. In essence, the nonlinear dissipation terms act as second- or third-order ACM-like operators instead of Harten's first-order ACM. The switch is used to signal the amount of nonlinear dissipation to be added to the high-order nondissipative scheme, one wave at a time. The base scheme is activated at all time. Thus, the current approach is also different in spirit from using ACM to sharpen the contact discontinuities in the original Harten second-order TVD scheme [6]. Now we discuss the filter numerical flux in more detail. It is of the form

$$\tilde{F}^*_{j+1/2,k} = \frac{1}{2}R_{j+1/2}\Phi^*_{j+1/2}. \quad (2.20)$$

This filter numerical flux $\tilde{F}^*_{j+1/2,k}$ should not be confused with the standard numerical flux $\tilde{F}_{j+1/2,k}$ for F_x in (2.18). $\tilde{F}^*_{j+1/2,k}$ is the modified form of the nonlinear dissipation portion of $\tilde{F}_{j+1/2,k}$. The elements of $\Phi^*_{j+1/2}$ denoted by $\phi^{l*}_{j+1/2}$ are

$$\phi^{l*}_{j+1/2} = \kappa\theta^l_{j+1/2}\phi^l_{j+1/2}. \quad (2.21)$$

$\phi^l_{j+1/2}$ in (2.21) are the elements of $\Phi^l_{j+1/2}$ in (2.19). The function $\kappa\theta^l_{j+1/2}$ is the key mechanism for achieving high accuracy of the fine scale flow structure as well as shock waves in a stable manner. In other words, the elements of $\Phi^*_{j+1/2}$ are the same as the nonlinear dissipation portion of the TVD or ENO scheme (2.19) with the exception of premultiplying by $\kappa\theta^l_{j+1/2}$. The parameter κ is problem dependent. For smooth flows, κ is used to improve nonlinear stability and can be very small. For the numerical examples in Section 3, different examples require a different value of κ because of the large variant of the flow property. The range of κ for these problems is $0.03 \leq \kappa \leq 2$. The function $\theta^l_{j+1/2}$ is the Harten switch. For a general $2m + 1$ points base scheme, Harten recommended

$$\theta^l_{j+1/2} = \max\left(\hat{\theta}^l_{j-m+1}, \ldots, \hat{\theta}^l_{j+m}\right), \tag{2.22}$$

$$\hat{\theta}^l_j = \left|\frac{\left|\alpha^l_{j+1/2}\right| - \left|\alpha^l_{j-1/2}\right|}{\left|\alpha^l_{j+1/2}\right| + \left|\alpha^l_{j-1/2}\right|}\right|^p. \tag{2.23}$$

Instead of varying κ for the particular physics, one can vary p. The higher the p, the less the amount of numerical dissipation is added. Note that by varying the $p \geq 1$ in (2.23), one can essentially increase the order of accuracy of the dissipation term. The order of the dissipation depends on the value of p (Bjorn Sjogreen, private communication, 1998). For all of the numerical examples, we use $p = 1$ and

$$\theta^l_{j+1/2} = \max\left(\hat{\theta}^l_j, \hat{\theta}^l_{j+1}\right). \tag{2.24}$$

The $\alpha^l_{j+1/2}$ are elements of $R^{-1}_{j+1/2}(U_{j+1} - U_j)$. The shock–turbulence interaction examples appear to favor this form of $\theta^l_{j+1/2}$.

Formulae for $\phi^l_{j+1/2}$ are well known and can be found in the literature. For illustration purposes, we show a form of the $\phi^l_{j+1/2}$ function in which all of the examples shown in Section 3 are used for the computations. We choose the Harten–Yee upwind TVD form, where

$$\phi^l_{j+1/2} = \frac{1}{2}\psi\left(a^l_{j+1/2}\right)\left(g^l_{j+1} + g^l_j\right) - \psi\left(a^l_{j+1/2} + \gamma^l_{j+1/2}\right)\alpha^l_{j+1/2}, \tag{2.25a}$$

$$\gamma^l_{j+1/2} = \frac{1}{2}\psi\left(a^l_{j+1/2}\right)\begin{cases}\left(g^l_{j+1} - g^l_j\right)/\alpha^l_{j+1/2} & \alpha^l_{j+1/2} \neq 0 \\ 0 & \alpha^l_{j+1/2} = 0.\end{cases} \tag{2.25b}$$

Other shock-capturing schemes with structure similar to (2.19) such as the symmetric TVD schemes (Yee [8, 9]) and Roe second-order upwind scheme (Roe [38]) are also applicable. The $a^l_{j+1/2}, l = 1, 2, 3, 4$, are the characteristic speeds of $\frac{\partial F}{\partial U}$ evaluated at some symmetric average of $U_{j,k}$ and $U_{j+1,k}$. The Roe's average is an example of this (Roe [39]). The function ψ is an entropy correction to $|a^l_{j+1/2}|$. One possible form is (Harten and Hyman [40])

$$\psi\left(a^l_{j+1/2}\right) = \begin{cases}\left|a^l_{j+1/2}\right| & \left|a^l_{j+1/2}\right| \geq \delta_1 \\ \left[\left(a^l_{j+1/2}\right)^2 + \delta_1^2\right]/2\delta_1 & \left|a^l_{j+1/2}\right| < \delta_1.\end{cases} \tag{2.25c}$$

For problems containing only unsteady shocks, δ_1 is usually set to zero. Note that entropy-violating phenomena occur only for steady or nearly steady shocks. For steady-state

problems containing strong shock waves, a proper control of the size of δ_1 is very important, especially for hypersonic blunt-body flows. See Yee *et al.* [32]) for a discussion.

Examples of the commonly used "limiter" function g_j^l can be expressed as

$$g_j^l = \text{minmod}\left(\alpha_{j-1/2}^l, \alpha_{j+1/2}^l\right), \tag{2.25d}$$

$$g_j^l = \left(\alpha_{j+1/2}^l \alpha_{j-1/2}^l + \left|\alpha_{j+1/2}^l \alpha_{j-1/2}^l\right|\right) / \left(\alpha_{j+1/2}^l + \alpha_{j-1/2}^l\right), \tag{2.25e}$$

$$g_j^l = \left\{\alpha_{j-1/2}^l\left[\left(\alpha_{j+1/2}^l\right)^2 + \delta_2\right] + \alpha_{j+1/2}^l\left[\left(\alpha_{j-1/2}^l\right)^2 + \delta_2\right]\right\} /$$
$$\left[\left(\alpha_{j+1/2}^l\right)^2 + \left(\alpha_{j-1/2}^l\right)^2 + 2\delta_2\right], \tag{2.25f}$$

$$g_j^l = \text{minmod}\left(2\alpha_{j-1/2}^l, 2\alpha_{j+1/2}^l, \tfrac{1}{2}\left(\alpha_{j+1/2}^l + \alpha_{j-1/2}^l\right)\right), \tag{2.25g}$$

$$g_j^l = S \cdot \max\left[0, \min\left(2\left|\alpha_{j+1/2}^l\right|, S \cdot \alpha_{j-1/2}^l\right), \min\left(\left|\alpha_{j+1/2}^l\right|, 2S \cdot \alpha_{j-1/2}^l\right)\right];$$
$$S = \text{sgn}\left(\alpha_{j+1/2}^l\right). \tag{2.25h}$$

Here δ_2 is a small dimensionless parameter to prevent division by zero and $\text{sgn}(\alpha_{j+1/2}^l) = \text{sign}(\alpha_{j+1/2}^l)$. In practical calculations $10^{-7} \leq \delta_2 \leq 10^{-5}$ is a commonly used range. For $\alpha_{j+1/2}^l + \alpha_{j-1/2}^l = 0$, g_j^l is set to zero in (2.25e). The minmod function of a list of arguments is equal to the smallest number in absolute value if the list of arguments is of the same sign, or is equal to zero if any arguments are of opposite sign. Later development in limiters have flooded the literature and has created much debate. Most of the improvements have been problem dependent. See Donat [34], Engquist and Sjogreen [33], and Jin and Lin [41] on the error propagation for nonlinear approximations to hyperbolic equations containing discontinuities in derivatives or discontinuous solutions.

2.3. Computer Implementation

To avoid additional logical statements in the actual coding and to promote parallelization, several of the forms with the potential of dividing by zero are modified. They are

$$\psi(z) = \sqrt{(\delta + z^2)}, \tag{2.26a}$$

$$\gamma_{j+1/2}^l = \frac{1}{2} \frac{\psi\left(a_{j+1/2}^l\right)\left(g_{j+1}^l - g_j^l\right)\alpha_{j+1/2}^l}{\left(\alpha_{j+1/2}^l\right)^2 + \epsilon}. \tag{2.26b}$$

We use the switch

$$\theta_j^l = \frac{\left|\left|\alpha_{j+1/2}^l\right| - \left|\alpha_{j-1/2}^l\right|\right|}{\left|\alpha_{j+1/2}^l\right| + \left|\alpha_{j-1/2}^l\right| + \epsilon}. \tag{2.26c}$$

In all of the computations, we take $\epsilon = 10^{-7}$. The value of δ was taken to be $1/16$ (unless indicated) to satisfy an entropy condition. However, the fine scale flow structure showed minor sensitivity to the value of this constant.

2.4. Other Applicable Base Schemes

There are other possible high-order base schemes that one can use. For example, the fifth-
or seventh-order upwind schemes and the 2–4 or 2–6 MacCormack scheme. If the fifth- or
seventh-order upwind schemes are used as base schemes, to reduce numerical dissipation,
one needs to *subtract* the dissipation portion of these upwind schemes *from the filter step*.
The dissipation portion of these upwind schemes can be obtained by rewriting the scheme
into two parts, a central part and the "rest." The "rest" is the dissipation portion. For the 2–4
or 2–6 MacCormack scheme, the time discretization is an integral part and one has to use
the complete scheme as the base scheme. For the filter step, one adds the filter numerical
fluxes as an added corrector step as described in Yee [8] or Yee and Shinn [42]. The filter
numerical flux is the same as (2.20) but the $\phi^l_{j+1/2}$ has a slightly different form to take into
account the Lax–Wendroff type of Δt^2 term. See Yee [8] or Young and Yee [43] for the
formula.

2.5. Other Applicable Characteristic Filters

MUSCL approach using an approximate Riemann solver. The filter numerical flux
function for an upwind MUSCL-type scheme as described in Yee [8] using an approximate
Riemann solver can be expressed as

$$\tilde{F}^*_{j+1/2,k} = \frac{1}{2} R^\circ_{j+1/2} \Phi^\circ_{j+1/2}. \tag{2.27a}$$

The elements of $\Phi^\circ_{j+1/2}$ and the vector $(\alpha^\circ)_{j+1/2}$ are given by

$$(\phi^\circ)^l_{j+1/2} = -\kappa (\theta^\circ)^l_{j+1/2} \psi \left((a^\circ)^l_{j+1/2} \right) (\alpha^\circ)^l_{j+1/2}, \tag{2.27b}$$

$$(\alpha^\circ)_{j+1/2} = (R^\circ)^{-1}_{j+1/2} \left(U^R_{j+1/2} - U^L_{j+1/2} \right), \tag{2.27c}$$

where $\psi \left((a^\circ)^l_{j+1/2} \right)$ can be $|(a^\circ)^l_{j+1/2}|$ or the same form as (2.25c). Here $(a^\circ)^l_{j+1/2}$ are the
eigenvalues and $R^\circ_{j+1/2}$ is the eigenvector matrix of $\frac{\partial F}{\partial U}$ evaluated using a symmetric average
between $U^R_{j+1/2}$ and $U^L_{j+1/2}$; i.e.,

$$(a^\circ)^l_{j+1/2} = a^l \left(U^R_{j+1/2}, U^L_{j+1/2} \right), \tag{2.27d}$$

$$R^\circ_{j+1/2} = R \left(U^R_{j+1/2}, U^L_{j+1/2} \right). \tag{2.27e}$$

The switch $(\theta^\circ)^l_{j+1/2}$ is the same as (2.22) and (2.23) except it is evaluated using a symmet-
ric average between $U^R_{j+1/2}$ and $U^L_{j+1/2}$. However, there are options in applying the limiters
for system cases. Namely, one can impose limiters on the conservative, primitive, or char-
acteristic variables. The U^R and U^L are the upwind-biased interpolation of the neighboring
$U_{j,k}$ values with slope limiters imposed.

MUSCL approach using the Lax–Friedrichs numerical flux. The filter numerical flux
function for a MUSCL-type approach using the higher-order Lax–Friedrichs numerical flux
(Yee [8, 10]) can be expressed as

$$\tilde{F}^*_{j+1/2,k,l} = \frac{1}{2} [\Phi^\circ_{j+1/2}], \tag{2.28a}$$

where $\Phi^\circ_{j+1/2}$ is

$$\Phi^\circ_{j+1/2} = -(a^\circ)^{\max}_{j+1/2} \overline{(U^R_{j+1/2} - U^L_{j+1/2})}, \tag{2.28b}$$

and $(a^\circ)^{\max}_{j+1/2}$ can be

$$(a^\circ)^{\max}_{j+1/2} = \chi(|u^\circ_{j+1/2}| + c^\circ_{j+1/2}), \tag{2.28c}$$

where $\frac{1}{2} \leq \chi \leq 1$. The overbar for the quantity $\overline{(U^R_{j+1/2} - U^L_{j+1/2})}$ means the Harten switch together with κ is applied to each element of the vector. However, the $\alpha^l_{j+1/2}$ in $\hat{\theta}^l_{j+1/2}$ are replaced with a jump in the the conservative variables $U^R_{j+1/2}$ and $U^L_{j+1/2}$. If primitive or other variables are used for the right and left states, the switch together with κ should be applied to the corresponding variables.

2.6. Filter Numerical Flux for Time Marching to Steady States

For time marching to the steady states, one usually needs to add a fourth-order dissipation to a second-order spatial differencing scheme (Beam and Warming [44]). For the present schemes using characteristic filters, in addition to the filter operator L_f, one might need to add a sixth-order dissipation to a fourth-order spatial base scheme and an eighth-order to a sixth-order spatial base scheme in regions away from shocks for stability and convergence. Let L_d be such an operator. Take the case of a Runge–Kutta time discretization as in Section 2.2.1. There are two ways to incorporate the L_d operator. One way is to incorporate it at every stage of the Runge–Kutta method. The other is to include it as part of the filter step (2.17), i.e.,

$$U^{n+1} = \widehat{U}^{n+1} + \Delta t L_f(F^*, G^*)_{j,k} + \Delta t L_d(\widehat{U}^{n+1})_{j,k}, \tag{2.29}$$

where $L_f(F^*, G^*)_{j,k}$ is the same as in (2.17). These two ways of applying the L_d operator are most likely problem dependent and time integrator dependent. Extensive numerical experimentation is needed. For LMM type of time integrators, L_d is used in conjunction with L_f as an additional dissipation, as discussed in Section 2.2.1.

To minimize the amount of L_d in the vicinity of shock waves, there should be a switching mechanism κ_d (different from κ in (2.21)) to turn off the L_d operator in the vicinity of shock waves. The L_d operator can be applied to the conservative, primitive, or characteristic variables. The simplest form is to apply L_d to the conservative variables. Alternatively, since all of the work in computing the average states and the characteristic variable is done for the L_f operator, one can apply the L_d operator on the characteristic variables instead of the conservative variable. In this case, the switching mechanism κ_d can be a vector so that it is more in tune with the shock detector of the approximate Riemann solver.

3. NUMERICAL EXAMPLES

In all of the computations the classical fourth-order Runge–Kutta time discretization is employed. The detailed programming allows the Euler and viscous terms to be computed using separate methods. The basic spatial schemes are (i) non-compact central, (ii) compact central, and (iii) predictor–corrector upwind or upwind biased. Non-compact schemes are the standard second-, fourth-, and sixth-order methods. Compact schemes are either the

TABLE 3.1
Notation for Numerical Methods

Method	Order (Euler)	Order (viscous)	Shock capturing	Artificial compression	Compact
CEN44	4	4	No	No	No
TVD22	2	2	Yes	No	No
TVD44	4	4	Yes	No	No
TVD66	6	6	Yes	No	No
ACM22	2	2	Yes	Yes	No
ACM44	4	4	Yes	Yes	No
ACM66	6	6	Yes	Yes	No
ACM44C	4	4	Yes	Yes	Yes
ACM66C	6	6	Yes	Yes	Yes

Note. Order of accuracy refers to the formal order of the base scheme.

standard symmetric fourth-order or the sixth-order Pade schemes. For the purposes of this paper we concentrate on the central schemes with the same order of accuracy and type of base scheme for the convection and viscous terms. Comparable accuracy was obtained with the upwind or upwind-biased schemes proposed by Hixon and Turkel [17]. The filter operator (2.16), in conjunction with (2.20)–(2.26), is used as a filter step at the end of the full Runge–Kutta time step. Hereafter, we refer to this approach as the ACM/TVD (or simply ACM) method, indicating the fact that only one type of TVD dissipation is used for the numerical study. The various combinations of schemes considered for numerical experiments are shown in Table 3.1. The notation shown in Table 3.1 will be used for discussing the results for different numerical schemes. Here, the notation "TVD" with the various orders attached at the end means the second-order TVD dissipation (without the ACM switch) is used as the filter with the indicated order of the base scheme for the convection and viscous terms. For simplicity of discussion, unless otherwise indicated, the term TVD or ACM scheme means the selected base schemes indicated in Table 3.1 using the TVD or ACM/TVD filter. Studies using ENO or WENO dissipation as filters are planned. Computations using the SHOEC splitting in conjunction with high-order central differencings as base schemes for a variety of perfect gas and nonequilibrium flow applications are also planned. It appears that the SHOEC splitting is more stable and requires less numerical dissipation.

Without introducing additional notation, for inviscid flow simulations the same notation is used except the viscous terms are not activated.

Five test cases are considered. The first two are inviscid and the last three are compressible DNS computations. These test cases are chosen to examine the versatility and accuracy of the proposed schemes for a variety of flows where most conventional methods exhibit difficulty in obtaining low-dissipative solutions in an efficient and stable manner. All the test cases use either a uniform or mildly stretched Cartesian grid in the y-direction. No attempt is made to enhance the resolution using appropriate adaptive grid procedures. At present, the code used for the test cases reduces to lower-order central base schemes near the boundary points since either these test cases employ periodic boundary condition or the effect of lower-order boundary schemes is illustrated. Stable boundary treatments suggested by Gustafsson and Olsson [4] should be used and are not yet implemented for the present study. Nonreflecting boundary conditions or characteristic inflow and outflow boundary treatment are also not implemented.

The five test cases are: (1) a stationary vortex evolution; (2) a horizontally convecting vortex, (3) a vortex pairing in a time-developing mixing layer with shock waves formed around the vortices; (4) a shock wave impinging on a spatially evolving mixing layer where the evolving vortices must pass through a shock wave, which in turn is deformed by the vortex passage; and (5) a 3-D compressible turbulent channel flow to validate that the proposed schemes are, in fact, capable of sustaining turbulence. To examine the resolution of the proposed schemes where shock waves are absent, the computation was compared with the CEN44 (the classical spatially fourth-order central differencing for the convection and diffusion terms) before shock waves were developed for the vortex pairing case. Good agreement was obtained.

Aside from evaluating the vortex preservation property, the performance of these schemes with the presence of shock waves and turbulence are evaluated based on the following factors:

(a) effect of the ACM term,
(b) effect of the order of the base scheme,
(c) effect of the grid size (grid refinement study),
(d) effect of employing a compact or non-compact base scheme,
(e) effect of the adjustable parameter κ for the particular physics,
(f) effect of the flux limiters,
(g) shear and fine scale flow structure capturing capability.

3.1. Isentropic Vortex Evolution

The first two test cases are chosen to assess the performance of the proposed schemes for evolution of a 2-D inviscid isentropic vortex in a free stream. Similar test cases have also been used by several authors for testing other schemes with respect to vortex preservation (Gerritsen [21], Davoudzadeh *et al.* [45], and Shu (private communication, 1996)). The mean flow velocity, u_∞ and v_∞; pressure, p_∞; and density, ρ_∞ are considered to be free stream. Test case 1 is a stationary (steady) vortex with $(u_\infty, v_\infty) = (0, 0)$, and case 2 is a horizontally convecting vortex with $(u_\infty, v_\infty) = (1, 0)$. In both cases $p_\infty = \rho_\infty = 1$.

As an initial condition, an isentropic vortex with no perturbation in entropy ($\delta S = 0$) is added to the mean flow field. The perturbation values are given by

$$(\delta u, \delta v) = \frac{\beta}{2\pi} e^{(1-r^2)/2}(-\bar{y}, \bar{x}), \tag{3.1}$$

$$\delta T = -\frac{(\gamma - 1)\beta^2}{8\gamma\pi^2} e^{1-r^2}, \tag{3.2}$$

where β is the vortex strength and $\gamma = 1.4$. Note that the vortex strength β should not be confused with the β in Section 2.1.2. Here $T = \frac{p}{\rho}$, $T_\infty = 1.0$, $(\bar{x}, \bar{y}) = (x - x_{v_0}, y - y_{v_0})$, where x_{v_0} and y_{v_0} are coordinates of the center of vortex initially, and $r^2 = \bar{x}^2 + \bar{y}^2$. The entire flow field is required to be isentropic so, for a perfect gas, $p/\rho^\gamma = 1$.

From the relations, $\rho = \rho_\infty + \delta\rho$, $u = u_\infty + \delta u$, $v = v_\infty + \delta v$, $T = T_\infty + \delta T$, and the above isentropic relation, the resulting state for conservative variables is given by

$$\rho = T^{1/(\gamma-1)} = (T_\infty + \delta T)^{1/(\gamma-1)} = \left[1 - \frac{(\gamma - 1)\beta^2}{8\gamma\pi} e^{1-r^2}\right]^{1/(\gamma-1)} \tag{3.3}$$

$$\rho u = \rho(u_\infty + \delta u) = \rho\left[1 - \frac{\beta}{2\pi}e^{(1-r^2)/2}\right] \tag{3.4}$$

$$\rho v = \rho(v_\infty + \delta v) = \rho\left[1 + \frac{\beta}{2\pi}e^{(1-r^2)/2}\right] \tag{3.5}$$

$$p = \rho^\gamma \tag{3.6}$$

$$e = \frac{p}{\gamma - 1} + \frac{1}{2}\rho(u^2 + v^2). \tag{3.7}$$

These two vortex problems provide a good test bed for evaluating the schemes performance with the absence of shock waves and turbulence. The exact solution with given initial states is just a passive convection of the vortex with the mean velocity and thus provides a good measure of the accuracy of the schemes for smooth solutions of the Euler equations. The initial vortex covers a domain of $0 \le x \le 10$ and $-5 \le y \le 5$.

Periodic boundary conditions (BCs) in both directions are traditionally used for these test cases. Since the code reduces to lower-order central base schemes near the boundary points, and nonreflecting BCs are not used, non-periodic BCs simulations would provide the opportunity to examine the effect of the sizes of computational boxes on preserving the vortex core during time evolution. Nonreflecting BCs and stable boundary treatments suggested by Gustafsson and Olsson [4] will be implemented for a future study.

Both test cases employ a uniform Cartesian grid. Density profiles at the centerline, $y = 0$, cutting through the center of the vortex of the various schemes are used for comparison. Data on the centerline was extracted up to 5 unit lengths away to the left and the right, from the location of the center of the vortex. In all of the computations for the vortex evolution, unless otherwise indicated, $\delta = 0.01$ (2.26a) and limiter (2.25f) are used.

3.1.1. Stationary Vortex

For the stationary vortex test case, a uniform grid spacing of $\Delta x = \Delta y = 0.125$, covering the domain of $0 \le x \le 50$ and $-5 \le y \le 5$, is used. The grid is 401×81. The vortex is placed at the center of the rectangle, $(x - x_{v_0}, y - y_{v_0}) = (25, 0)$. For reasons of economy, only the left and right boundaries in the x-direction are kept fairly distant from the center of the vortex core at 25 unit lengths. Only 5 unit lengths are used in the y-direction. Since there are no shock waves or steep gradient regions for this flow, the filter is used to stabilize the nonlinear governing equations. For this reason, the filter coefficient κ (2.21) should be kept very small. We use $\kappa = 0.05$ for all of the computations. The time step is also fixed with $\Delta t = 0.04$.

The density profiles across the vortex at the centerline, $y = 0$, for the various schemes are illustrated in Fig. 3.1. Figure 3.1 which shows the effect of increasing the accuracy from second- to fourth- and sixth-order using the TVD filter (TVD22, TVD44, and TVD66) compared with the ACM/TVD filter (ACM22, ACM44, and ACM66). Although the order of the viscous terms is indicated in the method, the viscous terms are not activated. Figure 3.1a compares the exact solution with the solutions obtained by the TVD22, TVD44, and TVD66 methods at $t = 50$ (after 1250 time steps). All of the TVD methods, regardless of the order of the base schemes, are very diffusive, especially around the vortex core. Higher-order base schemes exhibit slightly better resolution than the second-order base method. Figure 3.1b displays the same computation at a later time $t = 100$ (after 2500
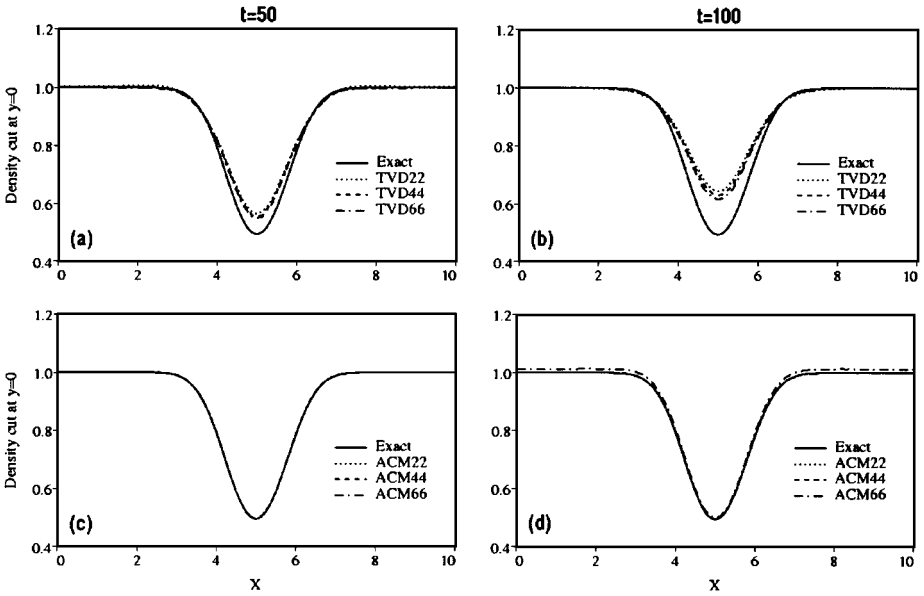
FIG. 3.1. Stationary vortex: comparison of the various orders of TVD and ACM methods with the exact solution, illustrated by density profiles at the centerline $y = 0$, at $t = 50$ and $t = 100$ for a 401×81 grid ($\kappa = 0.05$).

time steps). The computed vortex core is even more diffused compared with the exact solution.

Figures 3.1c and 3.1d show the same computation at $t = 50$ and 100 using the various orders of the base scheme with the ACM/TVD filter. These figures display the effect of the ACM/TVD filter on the vortex core. The ACM methods, regardless of the order, have not diffused the vortex core after $t = 50$. All numerical solutions fall almost on top of the exact solution, except for very small differences for the ACM66 method. At $t = 100$, the ACM66 resolution has been slightly displaced due to the boundary effects. However, the ACM22 and ACM44 remain quite accurate.

3.1.2. Horizontally Convecting Vortex

For the horizontally convecting vortex, again, a uniform grid spacing of $\Delta x = \Delta y = 0.125$, covering the domain of $0 \le x \le 110$ and $-5 \le y \le 5$, is used. The grid is 481×81 for $t = 50$ and 881×81 for $t = 100$. The vortex is initially placed at $(x - x_{v_0}, y - y_{v_0}) = (5, 0)$. The time step, $\Delta t = 0.04$, is fixed for all runs, as is the vortex strength, $\beta = 5$. The adjustable parameter, κ, is set equal to 0.05 as in case 1. The vortex is convected to the right by the mean flow velocity.

The physics of the present vortex evolution is similar to that of the stationary case, except the vortex is convecting. Since the ACM44 and ACM66 are less diffusive than the ACM22 for case 1, only the ACM44 and ACM66 are used for the present computation. Figure 3.2 displays density profiles across the centerline at $y = 0$, comparing the exact solution with the ACM44 and ACM66 methods at $t = 50$ and $t = 100$, and after 1250 and 2500 time steps, respectively. All numerical solutions are very accurate and fall almost on top of the exact solution. In these computations no visible boundary effects are seen because the right boundary of the domain in the direction of the vortex convection is initially kept relatively
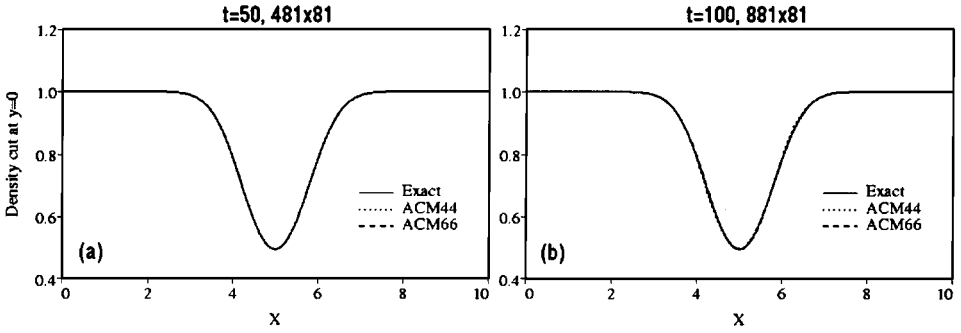
FIG. 3.2. Convecting vortex: comparison of ACM44 and ACM66 with the exact solution, illustrated by density profiles at the centerline $y = 0$, at $t = 50$ and $t = 100$ for a 481×81 and 881×81 grid, respectively ($\kappa = 0.05$).

far away. Although not visible from the density profiles, ACM44 exhibits small oscillatory solutions at $t = 100$. However, the ACM66 exhibits only small oscillations at the outer edge of the vortex. Figure 3.3 shows the density contours comparison of the exact solution with ACM44 and ACM66 at $t = 100$. We reran the same case using ACM44 and an increased $\kappa = 0.07$. The small oscillation disappeared and the solution is as accurate as for the ACM66 using $\kappa = 0.05$. Both ACM44 and ACM66 exhibit good vortex preservation. Figure 3.3 also shows the comparison of the two different values of κ using ACM44. These results indicate the effect of κ on the various orders of the ACM methods. For viscous flow, in the presence of shocks, shears and turbulence, the effect of κ on the resolution of fine scale flow structure plays a different role than for the inviscid flows with smooth solution. When we ran the same case using CEN44, the solution blew up at $t = 65$. We ran the same case using ACM44 with $\kappa = 0.07$ until $t = 200$, convected for 20 vortex diameters. The solution is still very accurate but slightly diffuse compared with the exact solution.

3.1.1. Boundary Effects on the Stationary Vortex

The effect of the size of the computational boxes was studied for the stationary vortex evolution, case 1. All the numerical experiments with the TVD and ACM methods discussed for case 1 were repeated on a smaller computational domain of $0 \le x \le 10$ and $-5 \le y \le 5$ for which the initial vortex touches the boundary of this smaller computational box. The grid spacings and time step are the same as before, except the grid is now 81×81. Figure 3.4 shows the computations on the reduced domain. Comparison with Fig. 3.1 clearly demonstrates the effect of the physical boundary distances in the x-direction. The discrepancies between corresponding results on the larger and smaller domains are more pronounced at
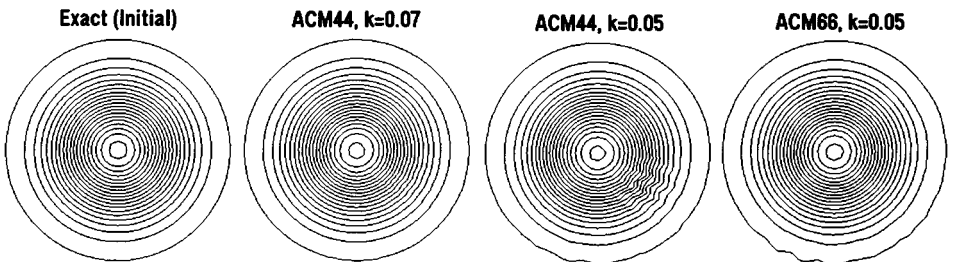

FIG. 3.3. Convecting vortex: comparison of the ACM44 and ACM66 with exact solution at $t = 100$ for $\kappa = 0.07$ and $\kappa = 0.05$, illustrated by density contour for a 881×81 grid.
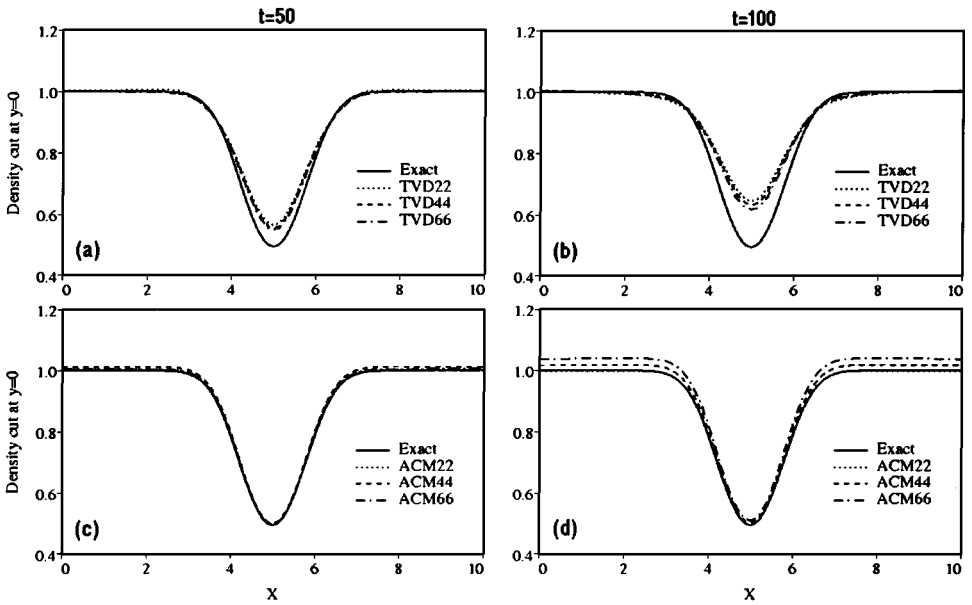
FIG. 3.4. Stationary vortex: comparison of various orders of TVD and ACM methods with the exact solution, illustrated by density profiles at the centerline $y = 0$, at $t = 50$ and $t = 100$ for a smaller computational box (81×81) showing the boundary effect ($\kappa = 0.05$).

$t = 100$ for the ACM methods. Figure 3.5 compares the numerical solution of the ACM66 method on larger and smaller domains with the exact solution.

Figure 3.6 displays the effect of the adjustable parameter κ in controlling the boundary effects (x-direction) for the ACM44 and ACM66 methods at $t = 100$. We reduced the κ value from 0.05 to 0.035 on the same smaller computational box. The profiles for both methods are on top of each other. The deviation from the exact solution of the computed solution due to boundary effects is less pronounced than for $\kappa = 0.05$. Figure 3.7 shows the effect of using different limiters (limiter (2.25f) vs limiter (2.25h)) at $t = 100$ on the same smaller computational box.
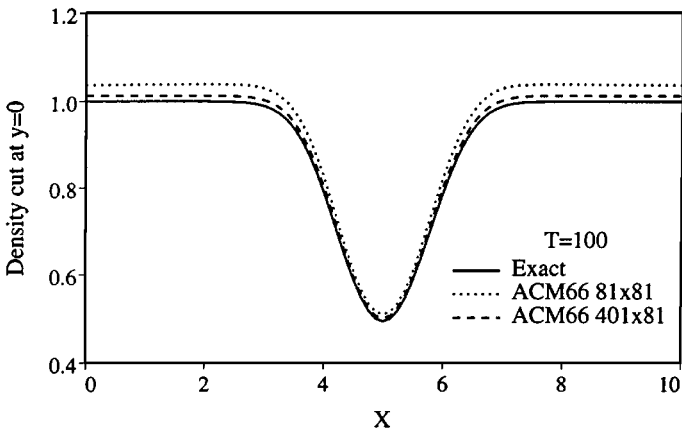
FIG. 3.5. Stationary vortex: comparison of the exact solution with ACM66 at $t = 100$ on the small computational box (81×81) and a larger computational box (401×81) ($\kappa = 0.05$).
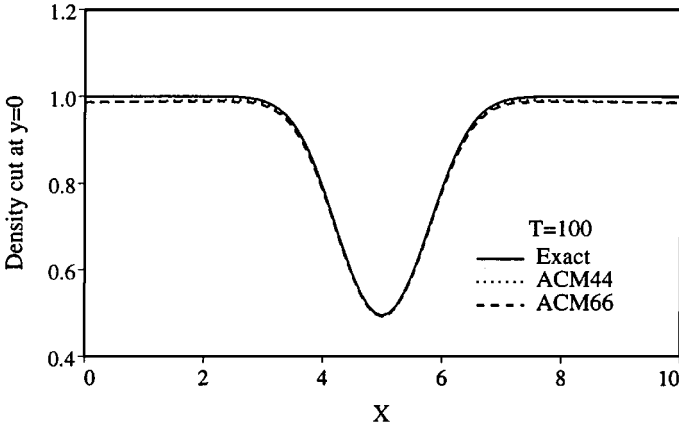
FIG. 3.6. Stationary vortex: comparison of the exact solution with ACM44 and ACM66 at $t = 100$ for the small computational box using a 81×81 grid ($\kappa = 0.035$).

3.2. Vortex Pairing in a Time-Developing Mixing Layer

This test case studied vortex growth and pairing in a temporal mixing layer at a convective Mach number equal to 0.8. At this Mach number there are shock waves (shocklets) that form around the vortices and the problem is to compute accurately the vortex evolution while avoiding oscillations around the shocks. Previous calculations of the problem can be found in Sandham and Reynolds [46], Lumpp [47], and Fu and Ma [48]. Figure 3.8 shows a schematic of the physical problem. Here we set up a base flow as in Sandham and Yee [49]

$$u = 0.5 \tanh(2y), \tag{3.8}$$

with velocities normalized by the velocity jump $u_1 - u_2$ across the shear layer and distances normalized by vorticity thickness,

$$\delta_\omega = \frac{u_1 - u_2}{(du/dy)_{\max}}. \tag{3.9}$$
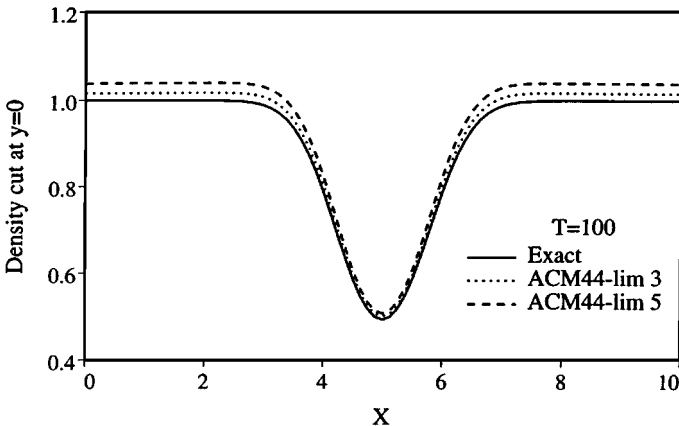
FIG. 3.7. Stationary vortex: comparison of the exact solution with ACM44 using two different flux limiters (lim3 (2.25f) and lim5 (2.25h)) at $t = 100$ for the small computational box using a 81×81 grid ($\kappa = 0.05$).
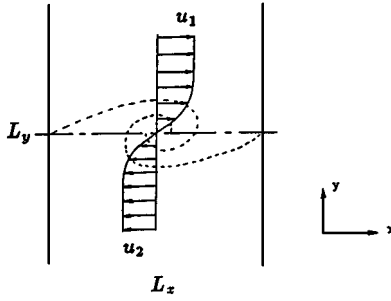
FIG. 3.8.   Schematic of the vortex pairing in a time-developing mixing layer.

Subscripts 1 and 2 refer to the upper ($y > 0$) and lower ($y < 0$) streams of fluid, respectively. The normalized temperature, and hence local sound speed squared, is determined from an assumption of constant stagnation enthalpy

$$c^2 = c_1^2 + \frac{\gamma - 1}{2}\left(u_1^2 - u^2\right).$$
(3.10)

Equal pressure through the mixing layer is assumed. Therefore, for this configuration of $u_2 = -u_1$ both fluid streams have the same density and temperature for $y \to \pm\infty$. The Reynolds number defined by the velocity jump, vorticity thickness, and kinematic viscosity at the free-stream temperature is set here to be 1000. The Prandtl number is set to 0.72, the ratio of specific heats is taken as $\gamma = 1.4$, and Sutherland's law with reference temperature $T_R = 300$ K is used for the viscosity variation with temperature. The reference sound speed squared, c_R^2, is taken as the average of c^2 over the two free streams.

Disturbances are added to the velocity components in the form of simple waves. For the normal component of velocity we have the perturbation

$$v' = \sum_{k=1}^{2} a_k \cos(2\pi k x/L_x + \phi_k) \exp(-y^2/b),$$
(3.11)

where $L_x = 30$ is the box length in the x-direction and $b = 10$ is the y-modulation. In our test case we simulate pairing in the center of the computational box, by choosing the initially most unstable wave $k = 2$ to have amplitude $a_2 = 0.05$ and phase $\phi_2 = -\pi/2$, and the subharmonic wave $k = 1$ with $a_1 = 0.01$ and $\phi_1 = -\pi/2$. The u-velocity perturbations are found by assuming that the total perturbation is divergence free. Even though these fluctuations correspond only approximately to eigenfunctions of the linear stability problem for a compressible mixing layer, they serve the purpose of initiating the instability of the mixing layer and have the advantage as a test case in that they can be easily coded.

Numerically the grid is equally spaced and periodic in the x-direction and stretched in the y-direction, using the mapping

$$y = \frac{L_y}{2}\frac{\sinh(b_y \eta)}{\sinh(b_y)},$$
(3.12)

where we take the box size in the y-direction $L_y = 100$, and the stretching factor $b_y = 3.4$. The mapped coordinate η is equally spaced and runs from -1 to $+1$. The boundaries at

$\pm L_y/2$ are taken to be slip walls. For example, at the lower boundary

$$\rho_1 = \rho_2, \tag{3.13a}$$

$$(\rho u)_1 = (\rho u)_2, \tag{3.13b}$$

$$(\rho v)_1 = 0, \tag{3.13c}$$

$$(e)_1 = [4(e)_2 - (e)_3]/3, \tag{3.13d}$$

where subscripts here refer to the grid point and e is the total energy.

3.2.1. Computational Results

We compute this test case on 401×401, 201×201, 101×101, and 41×41 grids. There is little to choose in the shock resolution properties with the variation in order of accuracy of the scheme since the proposed method will not improve the resolution of the shock waves over standard TVD or ENO schemes. We choose to compare temperature contours, which are most sensitive to oscillations (Lumpp, private communication), and accuracy of the fine scale structure. Figure 3.9 shows a snapshot of the temperature contours at $t = 40, 80, 120$, and 160 using ACM44, illustrating the roll-up of the primary vortices followed by vortex merging. Shock waves and shears form around the vortices with a peak Mach number ahead of the vortex of approximately 1.55 at $t = 120$. The grid is 201×201. The majority of the comparisons, however, use a 101×101 grid. In all of the computations for the vortex pairing case, unless indicated, limiter (2.25f) and $\delta = 1/16$ (2.26a) are used. The majority of the computations used $\kappa = 0.7$ (2.21) for the nonlinear fields for the ACM methods.

It is noted that a similar vortex pairing was used by Shu et al. [50] to evaluate the performance of high-order ENO schemes. The present results show superior performance over the result of Shu et al.
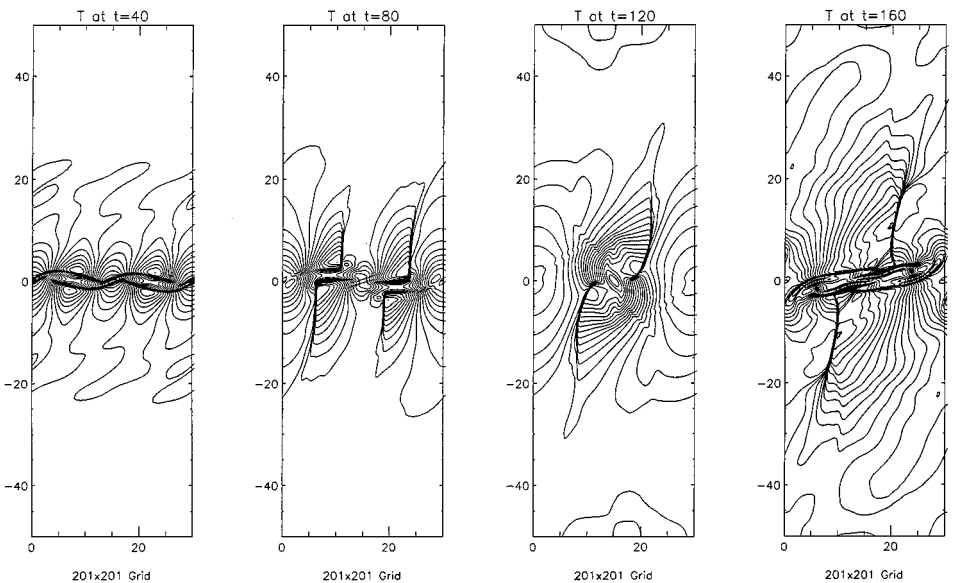

FIG. 3.9. Four stages in the vortex pairing, at times $t = 40, 80, 120, 160$, showing the temperature contours for a 201×201 grid with $\kappa = 0.7$ for the nonlinear fields and $\kappa = 0.35$ for the linear fields using ACM44.
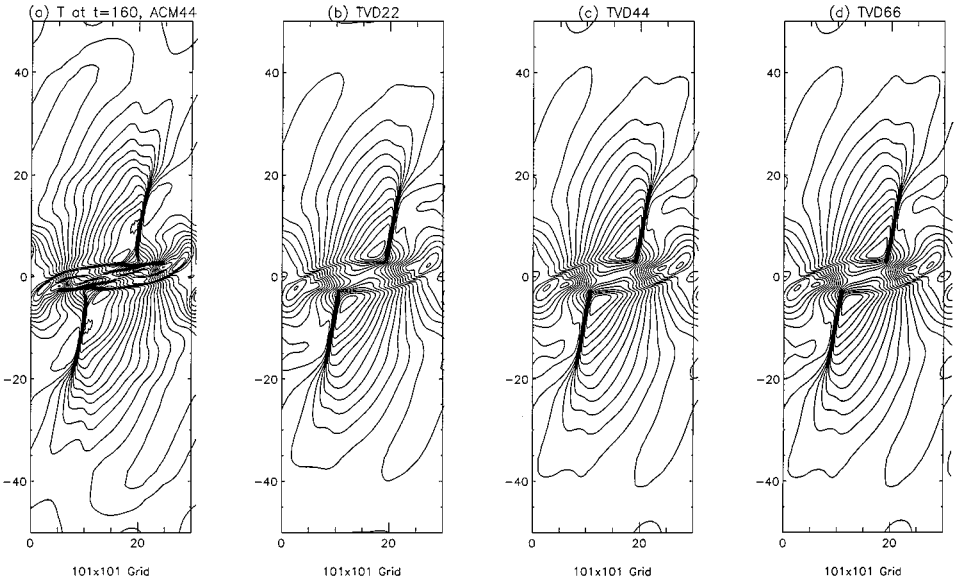
FIG. 3.10. Effect of order of accuracy on TVD methods (TVD22, TVD44, and TVD66), compared with the ACM44 solution at $t = 160$, illustrated by temperature contours at $t = 160$ for a 101×101 grid.

Effect of the ACM term and the order of the base scheme. Figure 3.10 shows the effect of increasing the accuracy from second to fourth and sixth order using the TVD filter (TVD22, TVD44, and TVD66). As can be seen there is almost no improvement as the order of accuracy is raised. Figure 3.11 shows the same plot using the ACM/TVD filter (ACM22,
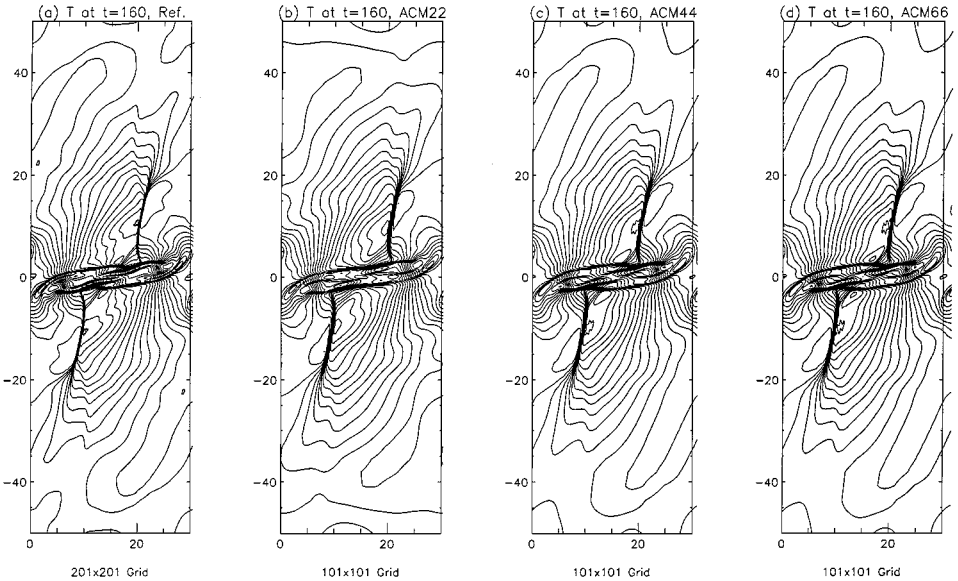
FIG. 3.11. Effect of order of accuracy on ACM methods (ACM22, ACM44, and ACM66) at $t = 160$ for a 101×101 grid compared with the reference solution (ACM44, 201×201 grid) using $\kappa = 0.7$ for the nonlinear fields and $\kappa = 0.35$ for the linear fields.

ACM44, and ACM66). Here there is an improvement, although the results even for the lowest order are quite good. All the ACM schemes capture the shock waves with minimal oscillations. Although not shown, the temperature contours for the TVD filter of various orders using a 101×101 grid are not nearly as accurate as the ACM44 using a 41×41 grid. (See the last plot of Fig. 3.12 of Yee *et al.* [51] or Sandham and Yee [2] for illustrations.) It can be seen that there is a significant advantage in moving from second to fourth order, but there is a smaller gain in moving from fourth to sixth order using TVD or ACM/TVD as a filter. (This is contrary to the isentropic vortex convection, where there are definite benefits of moving from fourth order to sixth order. The effect of order of accuracy is more pronounced for long-time integration of pure convection.) The fine scale flow structures are nearly resolved using a 101×101 grid compared with the reference solution using ACM44 and a 201×201 grid. Results from the ACM method are far superior to those from the standard TVD formulation. Note that there is no improvement in the shock resolution among the various orders of the base schemes, since the ACM term limited the amount of dissipation away from shocks and steep gradient areas, whereas the shock resolution is dictated by the flux limiter.

Effect of the grid size (grid refinement study).   To investigate the effect of order of the accuracy in more detail we consider simulations on a very coarse grid of 41×41 points. Such a case corresponds in practice to simulation of scales of turbulence arising from shear layers only two or three computational cells across. To ensure that the fine scale flow structure is fully resolved by the 201×201 reference grid, the same simulation was done on a 401×401 grid (figures not shown). The resolution of the ACM methods on a 41×41 grid is comparable to that of TVD methods on a 101×101 grid.

Effect of compact or non-compact base scheme.   For wave propagation and computational problems the performance of fourth- and sixth-order compact schemes, although more CPU intensive, appears to be superior to that of their non-compact cousin. For problems with shock waves the benefit of compact over non-compact schemes is less known due to the filter step. For this purpose we conduct similar experiments using (2.9) as base schemes. Results for the fourth- and sixth-order compact schemes are similar to results from the sixth-order non-compact scheme. Again there is little improvement compared with the fourth-order non-compact scheme. The compact schemes are almost double the CPU over their non-compact cousin for this 2-D compressible DNS computation using the fourth-order Runge–Kutta method. For this particular flow physics, a conclusion is that the use of the ACM in the filter step is essential to get the benefits of moving from second to fourth order, but even with the compact method as the base scheme, there is little benefit in moving to even higher-order base schemes. See Sandham and Yee [2] for illustrations. This is in contrast to the isentropic vortex convection where there are benefits of moving from fourth order to sixth order for long-time integration.

Effect of the adjustable parameter κ and shear and fine flow structure capturing capability.   The ACM switch has been demonstrated to give good shock resolution and to be essential if the benefits of higher-order discretization schemes are to be realized. There is, however, an adjustable parameter κ in the formulation, and results are sensitive to the precise choice of its value. Figures 3.12a and 3.12d illustrate the effect on the result using ACM44 for the pairing test case of reducing the parameter from 0.7 to 0.35. The vorticity and momentum thickness development is improved due to the reduction in numerical
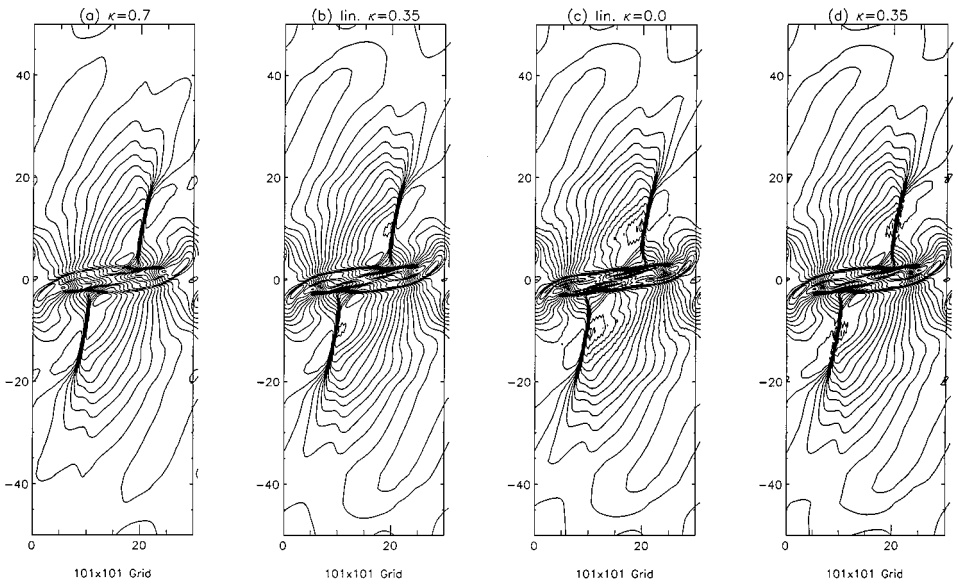
FIG. 3.12. Effect of κ in the ACM44 scheme on the fine scale flow structure, illustrated by temperature contours at $t = 160$: (a) $\kappa = 0.7$ for all fields; (b) $\kappa = 0.7$ for the nonlinear fields, and $\kappa = 0.35$ for the linear fields; (c) $\kappa = 0.7$ for the nonlinear fields and $\kappa = 0.0$ for the linear fields; and (d) $\kappa = 0.35$ for all fields for a 101×101 grid.

dissipation. From the temperature contours on Figs. 3.12a and 3.12d it can be seen that this has been achieved at the cost of formation of small oscillations around the shock wave. For the present problem one would be ready to pay this price to get the more accurate vortex evolution. However, in general it is not known how such numerically induced oscillations interact with small scales of turbulence. For the current method the correct procedure for a simulation of shock–turbulence interaction would be to find the smallest value of κ to resolve the shock waves satisfactorily and then increase the grid resolution until the turbulence is adequately resolved. There are perhaps other formulations of the ACM switch parameter κ based on the flow physics that can perform the adjustment to higher values automatically when stronger shock waves are present. This is a subject of future research.

To balance the shear and shock capturing, one alternative is to switch to a more compressive limiter (see Yee [31]) for the linear characteristics fields. Another alternative is to reduce the value of κ for the u, v linear fields. The comparison of using different values of κ for the linear and nonlinear fields is also shown in Fig. 3.12b and in Sandham and Yee [2].

Shock capturing schemes are designed to accurately capture shock waves, but with a less accurate capturing capability for contact discontinuities. In fact, the mixing layer seen at a large scale is a contact discontinuity. If one uses enough grid points to resolve the region of high shear in conjunction with the physical viscosity, it might not need to be "captured." Contact discontinuities relate to the characteristic velocities u and v. As an experiment, these linear characteristics were computed with no numerical dissipation. Filters were only applied to the nonlinear characteristic fields $u \pm c$ and $v \pm c$ using the ACM44 method. Interestingly, the computation was no less stable than that of the full TVD or ACM schemes. Figure 3.12c shows the resulting temperature field. It can be seen that good results were
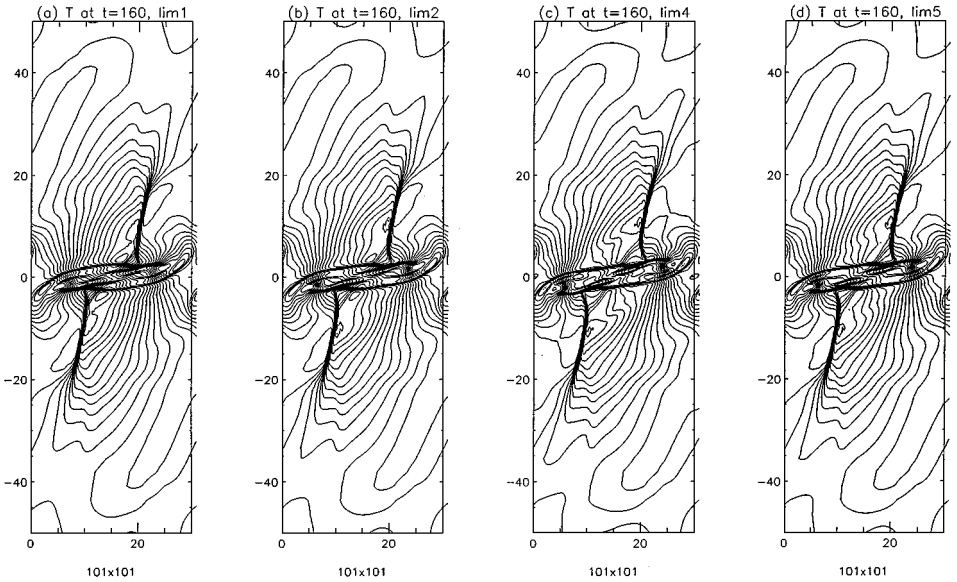
FIG. 3.13. Effect of flux limiters in the ACM44 scheme on the solution resolution, illustrated by temperature contours at $t = 160$: (a) lim1 (2.24d), (b) lim2 (2.24e), (c) lim4 (2.24g), and (d) lim5 (2.24h) for a 101×101 grid with $\kappa = 0.7$ for the nonlinear fields and $\kappa = 0.35$ for the linear fields.

obtained, although there is a trace of oscillation near the shock wave. This could be remedied by increasing κ slightly. However, the flow features of the shear and fine flow structure are accurately captured with similar resolution as the 201×201 grid with ACM44 applied to all of the characteristic fields. Comparison of the different $0.05 \le \kappa \le 2$ values for the nonlinear fields with the $\kappa = 0.0$ for the linear fields was also performed and the solution is very stable. See Yee *et al.* [51] for illustration.

Effect of the different flux limiters and the adjustable constant δ (2.26a). Figure 3.13 shows the comparison of the five classical flux limiters (2.25d)–(2.25h) (see Fig. 3.12a for lim3). Lim4 (2.25g) appears to perform the best with the λ shock, shear layer, and fine scale structure similar to those of the reference solution but using half of the grid size in each spatial direction. Figure 3.14 shows the effect of the various δ ((smu)^2 indicated on the plots) values on the fine scale flow structure capturing. It appears that $\delta = 0$ perform the best, except in this case the TVD filter is technically entropy violating. For this computation κ is set to 0.7 for all characteristic fields.

3.2.2. First-Order Upwind Dissipation As Characteristic Filter Computations

To examine the performance of using first-order dissipation as characteristic filters for high-order base schemes, we considered an entropy modification of Roe's first-order dissipation by redefining $\phi^l_{j+1/2}$ in (2.21) to be

$$\phi^l_{j+1/2} = -\psi\left(a^l_{j+1/2}\right)\alpha^l_{j+1/2}. \tag{3.14}$$

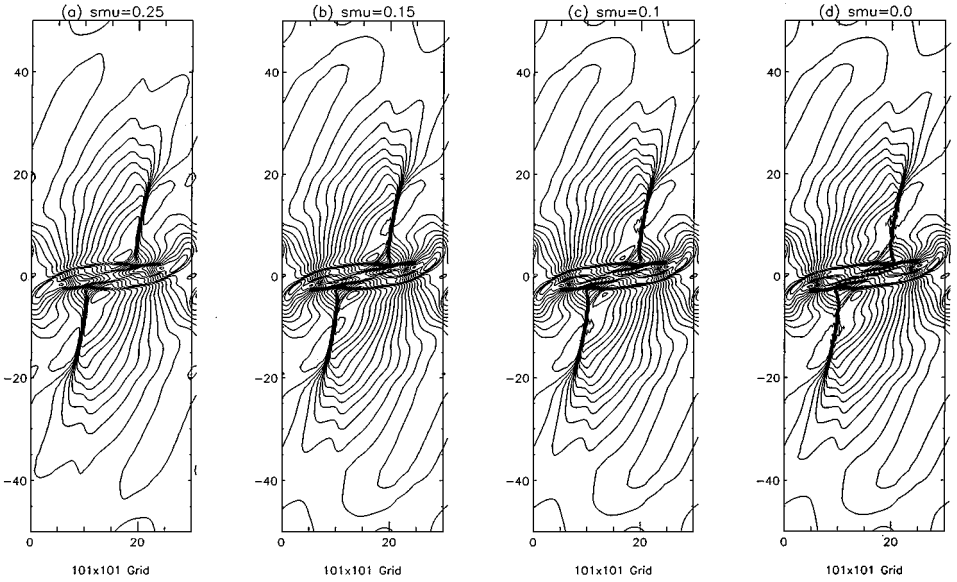Figure 3.15 shows the computation using the modified Roe's first-order dissipation as a

FIG. 3.14. Effect of δ $((\text{smu})^2)$ in the ACM44 scheme on the solution resolution, illustrated by temperature contours at $t = 160$: (a) $\delta = 1/16$, (b) $\delta = 0.0225$, (c) $\delta = 0.01$, and (d) $\delta = 0.0$ for a 101×101 grid with $\kappa = 0.7$ for all fields.

filter with the various orders of central differencing base scheme denoted by ACM22/1st, ACM44/1st, and ACM66/1st. The δ is set equal to $1/16$ using (2.26a) for $\psi(a^l_{j+1/2})$. The result is comparable to TVD22, TVD44, and TVD66. Rerunning the same case with a smaller δ results in more accuracy than using $\delta = 1/16$.
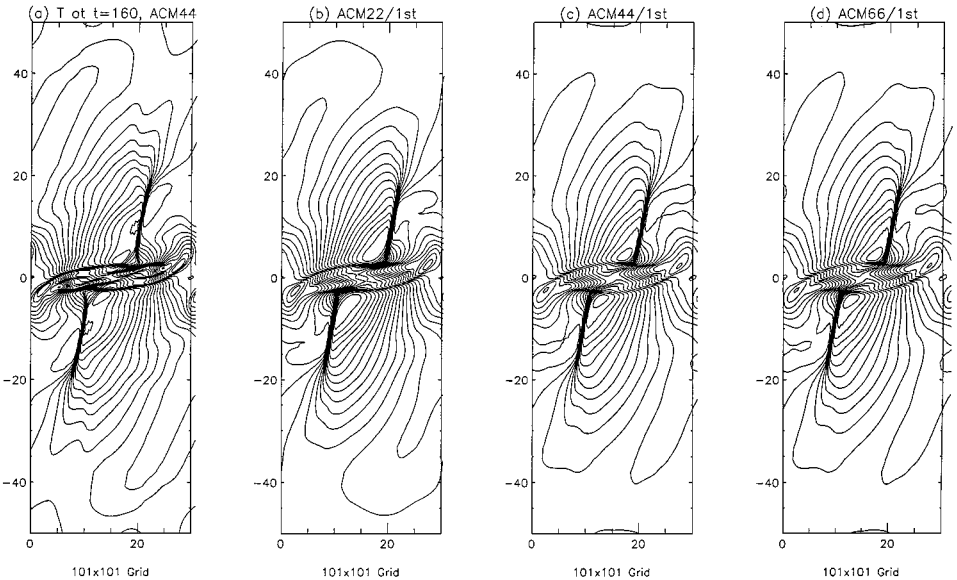
FIG. 3.15. Effect of order of accuracy (using the first-order dissipation filter) on ACM22/1st, ACM44/1st, and ACM66/1st on the solution resolution, illustrated by temperature contours at $t = 160$: (a) ACM44, (b) ACM22/1st, (c) ACM44/1st, and (d) ACM66/1st for a 101×101 grid with $\kappa = 0.7$ for the nonlinear fields and $\kappa = 0.35$ for the linear fields.

3.2.3. *Lax–Wendroff-Type TVD Dissipation As Characteristic Filter Computations*

To examine the applicability of using the Lax–Wendroff-type TVD dissipation filter, we recompute Fig. 3.11 using

$$\phi^l_{j+1/2} = \sigma\left(a^l_{j+1/2}\right)\left(g^l_{j+1} + g^l_j\right) - \psi\left(a^l_{j+1/2} + \gamma^l_{j+1/2}\right)\alpha^l_{j+1/2}, \tag{3.15a}$$

$$\sigma^l_{j+1/2} = \frac{1}{2}\left[\psi\left(a^l_{j+1/2}\right) - \frac{\Delta t}{\Delta x}\left(a^l_{j+1/2}\right)^2\right] \tag{3.15b}$$

$$\gamma^l_{j+1/2} = \sigma\left(a^l_{j+1/2}\right)\begin{cases} \left(g^l_{j+1} - g^l_j\right)/\alpha^l_{j+1/2} & \alpha^l_{j+1/2} \neq 0 \\ 0 & \alpha^l_{j+1/2} = 0 \end{cases}. \tag{3.15c}$$

In other words, using the Lax–Wendroff TVD dissipation as a filter involves an extra $\frac{\Delta t}{\Delta x}(a^l_{j+1/2})^2$ term in the ψ function compared with (2.25). This term is due to the U_{tt} term in the Lax–Wendroff formulation. Note that the use of (3.15) is not consistent in two ways. First, the base scheme uses Runge–Kutta time integrator and the filter step uses the Lax–Wendroff type of mixed space and time formulation. Second, for 2-D, one has to use the Strang [23] type of splitting to retain second-order time accuracy.

Disregarding the inconsistency, Figure 3.16 shows a comparison of the various orders of base schemes using (3.15) together with the ACM switch, denoted by ACM22/v^2, ACM44/v^2, and ACM66/v^2. The solutions are more diffusive but slightly more stable than the corresponding cases without the v^2 term (Fig. 3.11). Although the use of (3.15) is not consistent, the results are far superior to the TVD22, TVD44, and TVD66 methods (Fig. 3.10).
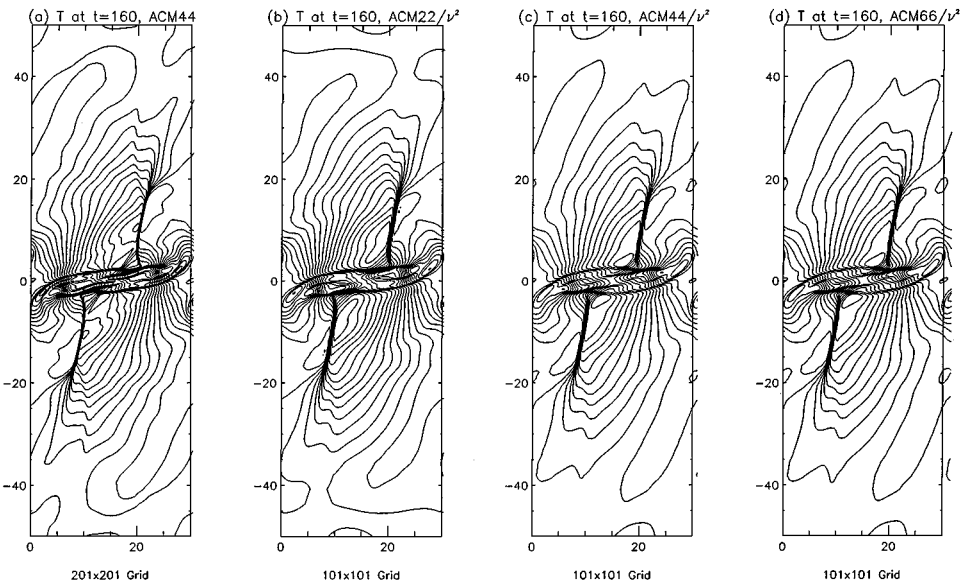

FIG. 3.16. Effect of order of accuracy on ACM22/v^2, ACM44/v^2, and ACM66/v^2 on the solution resolution, illustrated by temperature contours at $t = 160$: (a) ACM44, (b) ACM22/v^2, (c) ACM44/v^2, and (d) ACM66/v^2 for a 101×101 grid with $\kappa = 0.7$ for the nonlinear fields and $\kappa = 0.35$ for the linear fields.
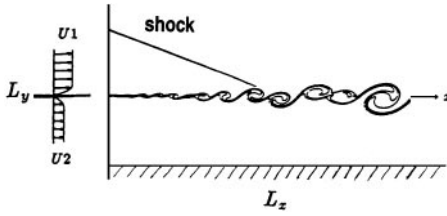
FIG. 3.17. Schematic of the shock Impingement on a spatially developing mixing layer.

3.3. Shock Wave Impingement on a Spatially Evolving Mixing Layer

The fourth test case has been developed to test the behavior of the schemes for shock waves interacting with shear layers where the vortices arising from shear layer instability are forced to pass through a shock wave. Figure 3.17 shows the schematic of the physical problem. An oblique shock is made to impact on a spatially developing mixing layer at an initial convective Mach number of 0.6. The shear layer vortices pass through the shock system and later through another shock, imposed by reflection from a (slip) wall at the lower boundary. The problem has been arranged with the Mach number at the outflow boundary everywhere supersonic so that no explicit outflow boundary conditions are required. This allows us to focus on properties of the numerical schemes rather than on the boundary treatment.

Figure 3.18 illustrates the nature of the flow on a 641×161 grid illustrating the pressure, density, and temperature fields using the ACM44 method and limiter (2.25f) with $\kappa = 0.35$
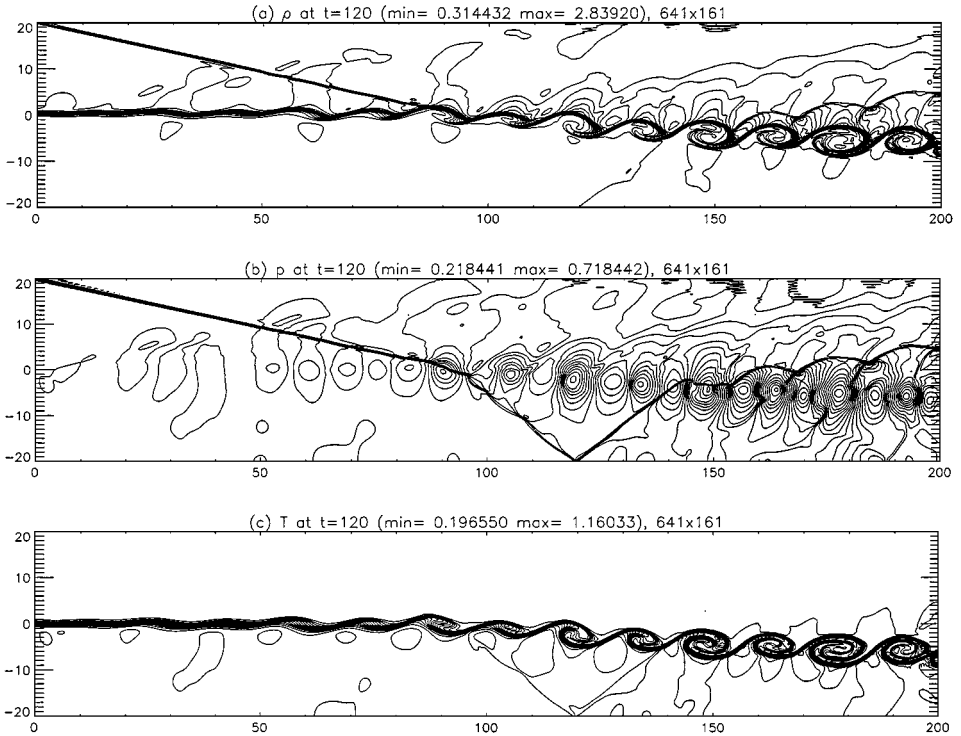

FIG. 3.18. The reference solution for the shock–shear–layer interaction problem at $t = 120$. Contours are shown of (a) pressure, (b) density, and (c) temperature for a 641×161 grid with $\kappa = 0.7$ for the nonlinear fields and $\kappa = 0.35$ for the linear fields.

for nonlinear characteristic fields and $\kappa = 0.175$ for the linear characteristic fields. The parameter δ is set to 0.25. This computation is used as the reference solution. An oblique shock originates from the top left-hand corner and this impacts on the shear layer at around $x = 90$. The shear layer is deflected by the interaction. Afterward we have a shock wave below the shear layer and an expansion fan above it. The shock wave reflects from the lower solid wall and passes back through the shear layer. The lower wall uses a slip condition so no viscous boundary layer forms and we focus on the shock-wave interaction with the unstable shear layer. The full no-slip problem would, however, make a challenging test case for the future.

The inflow is specified again with a hyperbolic tangent profile, this time as

$$u = 2.5 + 0.5 \tanh(2y), \tag{3.16}$$

giving a mixing layer with upper velocity $u_1 = 3$, lower velocity $u_2 = 2$, and hence a velocity ratio of 1.5. Equal pressures and stagnation enthalpies are assumed for the two streams, with convective Mach number, defined by

$$M_c = \frac{u_1 - u_2}{c_1 + c_2}, \tag{3.17}$$

where c_1 and c_2 are the free stream sound speeds equal to 0.6. The reference density is taken as the average of the two free streams and a reference pressure as $(\rho_1 + \rho_2)(u_1 - u_2)^2/2$. This allows one to compute the inflow parameters as given in the first two columns of Table 3.2. Inflow sound speed squared is found from the relation for constant stagnation enthalpy (3.10).

The upper boundary condition, given in column 3 of Table 3.2, is taken from the flow properties behind an oblique shock with angle $\beta = 12°$. The table also gives the properties behind the expansion fan (column 4) and after the oblique shock on the lower stream of fluid (column 5) computed by standard gasdynamics methods with $\beta = 38.118°$. In practice, the conditions in regions 4 and 5 do not correspond exactly to the simulations due to the finite thickness of the shear layer. The Mach number of the lower stream after this shock is approximately $M_5 = 1.6335$ and remains supersonic through all the successive shocks and

TABLE 3.2
Flow Properties for the Shock-Wave/Shear-Layer Test Case
in Various Regions of the Flow

Property	(1)	(2)	(3)	(4)	(5)
u-velocity	3.0000	2.0000	2.9709	2.9792	1.9001
v-velocity	0.0000	0.0000	−0.1367	−0.1996	−0.1273
θ (°)	0.0000	0.0000	2.6343	3.8330	3.8330
Density ρ	1.6374	0.3626	2.1101	1.8823	0.4173
Pressure p	0.3327	0.3327	0.4754	0.4051	0.4051
Sound speed c	0.5333	1.1333	0.5616	0.5489	1.1658
Mach number $|M|$	5.6250	1.7647	5.2956	5.4396	1.6335

Note. (1) upper stream inflow; (2) lower stream inflow; (3) upper stream after oblique shock; (4) upper stream after expansion fan; (5) lower stream after shock wave.

expansion fans up to the outflow boundary. The resulting shock waves are not strong, but tests showed that they could not be computed without using shock-capturing techniques. The lower boundary was specified with the same slip condition used for the pairing case (Eq. (3.13)).

The Prandtl number and ratio of specific heats were taken to be the same as for the vortex pairing test case. The Reynolds number was chosen to be 500.

Fluctuations are added to the inflow as

$$v' = \sum_{k=1}^{2} a_k \cos(2\pi k t/T + \phi_k) \exp(-y^2/b), \qquad (3.18)$$

with period $T = \lambda/u_c$, wavelength $\lambda = 30$, convective velocity $u_c = 2.68$ (defined by $u_c = (u_1 c_2 + u_2 c_1)/(c_1 + c_2)$), and $b = 10$. For $k = 1$ we take $a_1 = 0.05$ and $\phi = 0$, and for $k = 2$ we take $a_2 = 0.05$ and $\phi = \pi/2$. No perturbations are added to the u-component of velocity.

The grid is taken to be uniform in x and stretched in y according to Eq. (3.12) with $b_y = 1$. This stretching is much milder than for the pairing problem, as we have to resolve the shear layer even when it deflects away from $y = 0$. The box lengths were taken to be $L_x = 200$ and $L_y = 40$.

The reference solution indicates that vortex cores are located by low-pressure regions and the stagnation zones between vortices by high-pressure regions. The shock waves are seen to be deformed by the passage of the vortices. Another interesting observation is the way the core of the vortex at $x = 148$ has been split into two by its passage through the reflected shock wave. In spite of the relatively high amplitude chosen for the subharmonic inflow perturbation there is no pairing of vortices within the computational box. We do, however, begin to see eddy shock waves around the vortices near the end of the computational box where the local convective Mach number has increased to around 0.66. The oscillations seen near the upper boundary for $x > 120$ occur where the small Mach waves from the initial perturbations arrive at the upper boundary. The use of characteristic boundary conditions should remove this problem. Practically, the amplitude of oscillations is not sufficient to cause numerical instability or affect the remainder of the flow.

The test case was also run on a grid of 321×81 with $\Delta t = 0.12$, $\delta = 1/16$, and $\kappa = 0.35$ up to $t = 120$. Figures 3.19 and 3.20 show the effect of increasing the accuracy of the base scheme using the TVD and ACM/TVD filters. Again it can be seen that the ACM switch is essential for obtaining good vortex evolution (additionally, better shock resolution is obtained). For a more quantitative comparison, see Figs. 18 and 19 of Sandham and Yee [2]. From Fig. 3.19 it is apparent that all the standard TVD schemes, of whatever order, miss the correct vortex formation. From Figs. 3.19 and 3.20 there is a definite benefit in moving from second- to higher-order differencing, both in the amplitude of the fluctuations and in the correct convective velocity of the vortices. Figure 3.21 shows the effect of the δ values on the fine scale flow structure capturing. For this computation $\kappa = 0.35$ is used for all characteristic fields.

Disregarding the inconsistency, Fig. 3.22 shows a comparison of TVD44/v^2 with ACM44/v^2 on two grids. The solutions are again more diffusive but slightly more stable than the corresponding cases without the v^2 term. Although the use of (3.15) together with the ACM switch is not consistent, the results are far superior to TVD44 using (3.15) or (2.25) without the ACM switch.
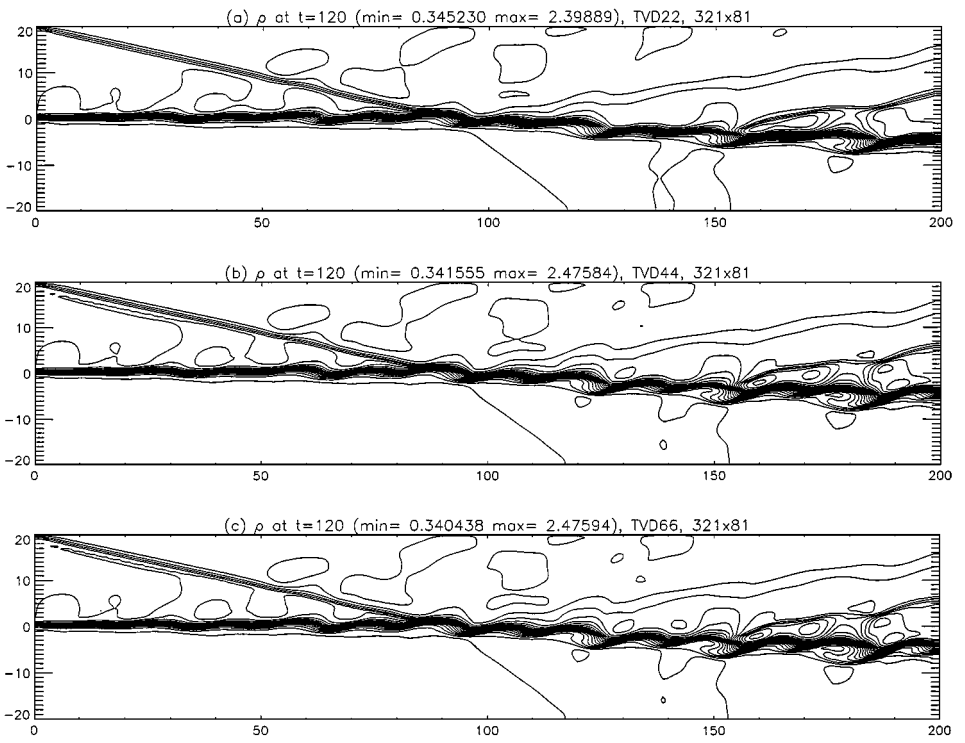
FIG. 3.19. Comparison of density contours at $t = 120$ for the shock–shear–layer test case: (a) TVD22, (b) TVD44, and (c) TVD66 for a 321×81 grid.
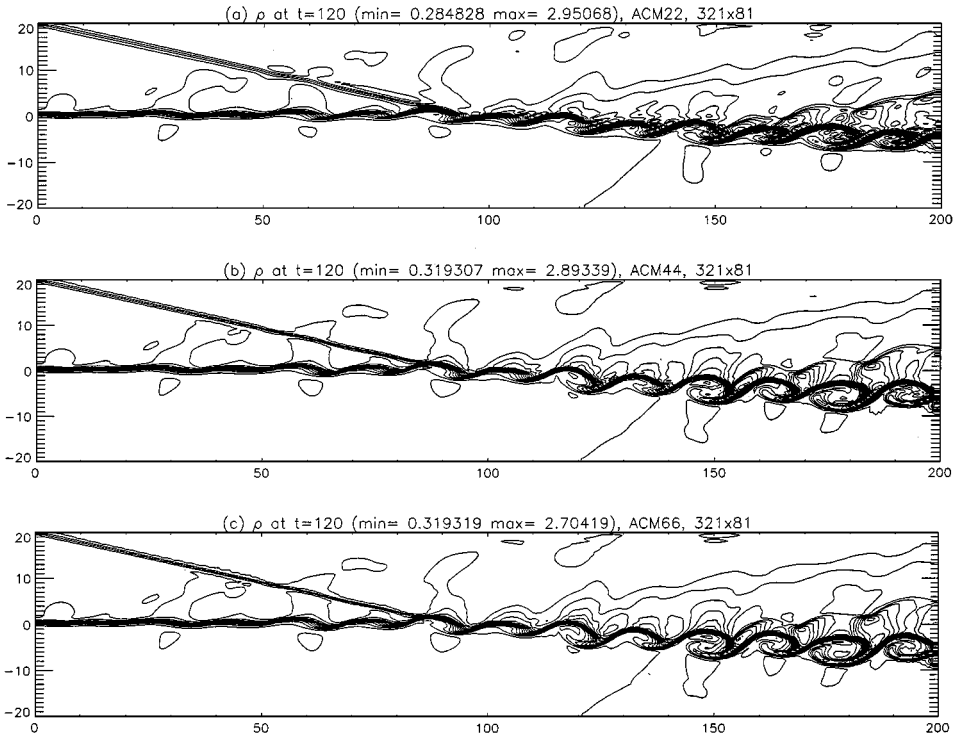

FIG. 3.20. Comparison of density contours at $t = 120$ for the shock–shear–layer test case: (a) ACM22, (b) ACM44, and (c) ACM66 for a 321×81 grid with $\kappa = 0.7$ for the nonlinear fields and $\kappa = 0.35$ for the linear fields.
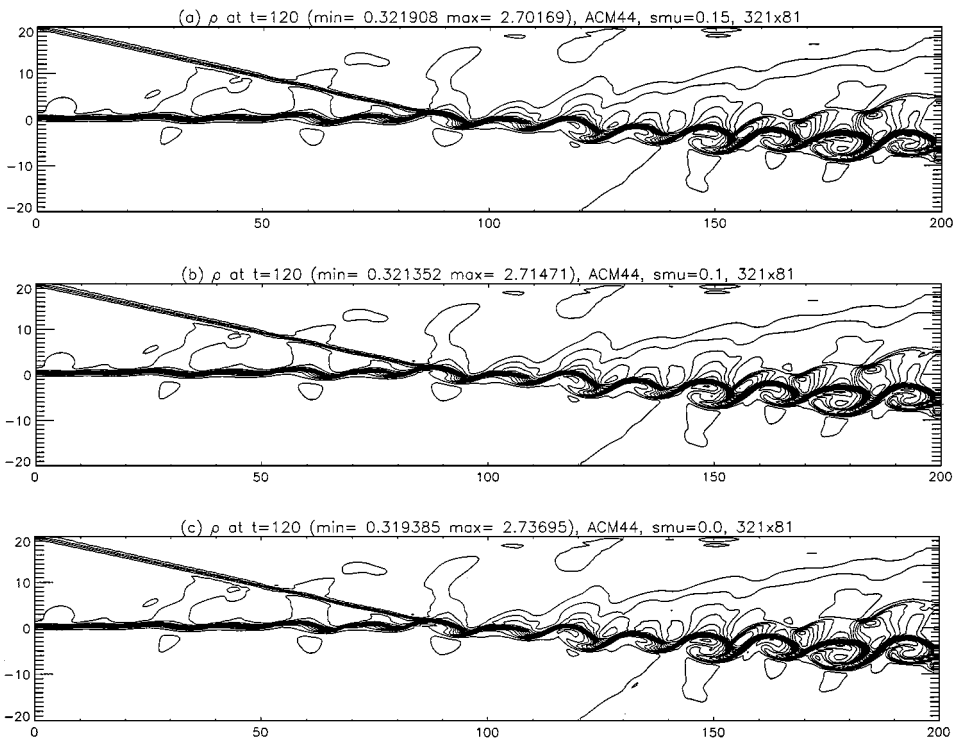
FIG. 3.21. Effect of δ ((smu)^2) in the ACM44 scheme on the solution resolution, illustrated by density contours at $t = 120$: (a) $\delta = 0.0225$, (b) $\delta = 0.01$, (c) $\delta = 0.0$ for a 321×81 grid with $\kappa = 0.7$ for all fields.
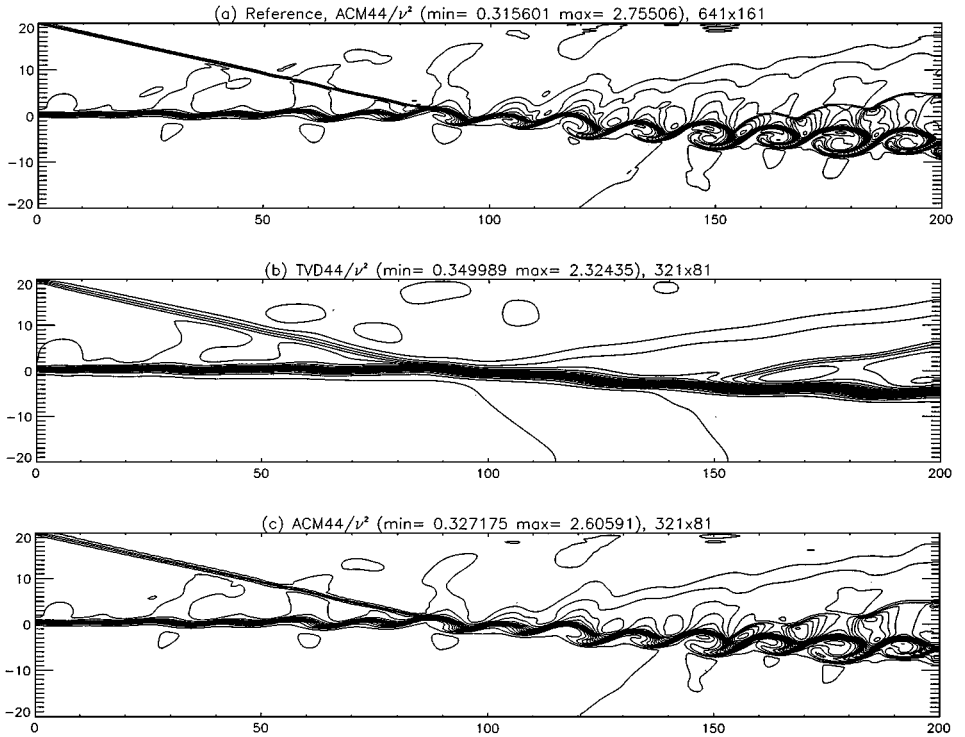

FIG. 3.22. Comparison of density contours at $t = 120$: (a) ACM44/ν^2 (641×161), (b) TVD44/ν^2 (321×81), and (c) ACM44/ν^2 (321×81) with $\kappa = 0.7$ for all fields.

233

3.4. Compressible Turbulent Channel Flow

As a final topic we consider the numerical simulation of three-dimensional turbulence. Given the additional numerical dissipation of shock-capturing schemes, even where shock waves are not present, it seems prudent to use this test case to validate that the new schemes proposed here are in fact capable of sustaining turbulence, before moving to complete simulations of shock–turbulence interactions. The case that we choose is similar to that of Coleman *et al.* [52]. In this problem we choose to normalize distances with half the separation between the walls, densities with the average density $\bar{\rho}$, velocities with the friction velocity u_τ, and temperature with the fixed wall temperature T_w. We take the pure pressure-driven flow, where forcing terms corresponding to $dp/dx = -1$ are added to the x-momentum equation. For a computational domain we use a box size with a streamwise length of 3 (channel half widths) and spanwise length of 1.5. While it is not sufficient for the two-point correlation to fall to zero, these box lengths are adequate for common turbulence statistics, as illustrated in Table 3.3, which compares the standard incompressible results of Kim *et al.* [53] with incompressible data computed by the first author with a fully spectral code on the small grid. It is likely that the same size domain will be a suitable test case for compressible flow provided the Mach number is low. At higher Mach numbers it is known [52] that correlation lengths increase. The advantage of the small domain calculation as a test case for numerical methods is the small memory requirement, making it feasible to run the calculations on workstations with limited memory.

For the compressible calculation we take the Mach number based on the friction velocity and sound speed corresponding to wall temperature to be 0.05, giving a centerline Mach number of approximately 1.1. A full grid-refinement study has not yet been attempted for this configuration. Results have been prepared for a grid of $32 \times 81 \times 32$, which is the same as that which has proved sufficient for good statistics up to triple moment budgets for the fully spectral code (Sandham and Howard [54]). The ACM44 method was applied with $\kappa = 0.35$ as in previous sections. The turbulence was indeed able to sustain itself, allowing the accumulation of statistical quantities for the flow. Figure 3.23a shows the mean velocity profile compared with the standard law of the wall (with Karman constant 0.41 and additive constant 5.5). The shift of the curve upward relative to the incompressible result is consistent with the findings of Coleman *et al.* Figure 3.23b shows the Favre-averaged stress $-\overline{\rho u'' v''}$ and the total stress found by adding the contribution $\mu d\bar{u}/dy$. The total stress must equal the non-dimensional y coordinate for the statistically converged flow. Favre averages are defined using mass weighting as $\tilde{u} = \overline{\rho u}/\bar{\rho}$ and fluctuations given by $u'' = u - \tilde{u}$. A detailed study will be reported in a future paper.

TABLE 3.3
Comparison of Incompressible Channel Flow Statistics between Large and Small Domain Calculations

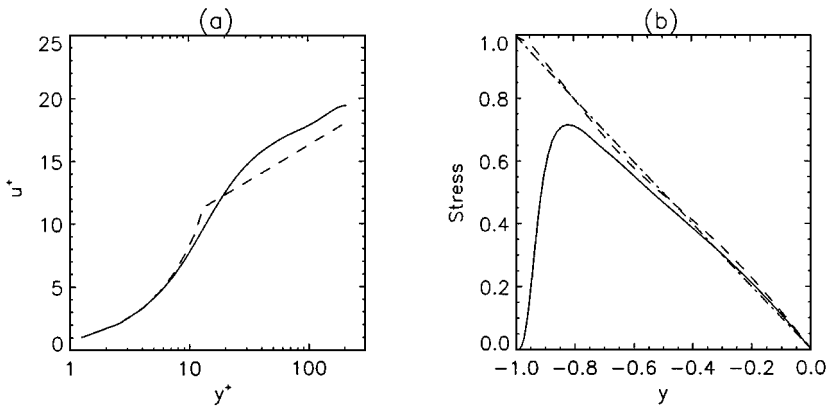| Property	[8]	Small domain
Centerline velocity	18.20	18.23
Mean velocity	15.63	15.69
Shape factor	1.62	1.61
Skin friction	0.00818	0.00811

FIG. 3.23. Compressible turbulent channel flow: (a) mean velocity profile (solid line) compared to the linear law $u^+ = y^+$ and the semi-logarithmic law of the wall, with Karman constant 0.41 and additive constant 5.5, and (b) Favre-averaged (solid line) and total stresses (dashed line) compared to the linear result (chain dotted line).

3.5. Computational Costs

For the DNS computations using the fourth-order Runge–Kutta method, the non-compact base schemes with the ACM/TVD filter are only around 25% more expensive than the same base schemes without ACM/TVD filter. This has been achieved by only requiring one application of the ACM/TVD filter per full time step for the convection terms. For LMM time discretizations, the non-compact base scheme with the ACM/TVD filter is only 10% more expensive than standard second-order TVD schemes.

For the Cray C90 it was found that the compact schemes were significantly more expensive, but this result was distorted for the present code by incomplete vectorization. An extra cost of around 2/3 is expected from considerations of operations count.

4. CONCLUSIONS

A generalization of the work of Gustafsson and Olsson and the ACM switch of Harten to a class of versatile low-dissipative high-order shock-capturing methods using characteristic based filters is proposed. The design principle of these schemes consists of two steps. The first step is the high-order spatial and temporal base scheme. A variety of standard high-order non-dissipative or low-dissipative base schemes fits in the present framework. The second step is the appropriate filter for stability and shocks, shear layers, and fine scale flow structure capturing. Many of the TVD, positive, WENO, and ENO dissipations, after a minor modification, are suitable candidates as filters. The final grid stencil of these schemes is five if second-order TVD schemes are used as filters and seven if second-order ENO schemes are used as filters for a fourth-order base scheme. Numerical boundary condition treatment is simple and can be the same as for the existing base and filter schemes.

The reason for proposing filter operators that have similar width of grid stencils as the base scheme is for efficiency and ease of numerical boundary treatment. Higher-than-third-order filter operators are applicable, but they are more CPU intensive and require special treatment near boundary points for stability and accuracy. It is well-known that near shocks and shears, the resolution of higher-than-third-order TVD or ENO schemes is comparable to their lower-order cousin except with a slight gain in resolution near steep gradients

and smooth flows. The five test cases show that an increased in resolution with improved efficiency can be accomplished if we limit the proper amount of numerical dissipation away from shocks and shears to stabilize the non-dissipative nature of the high-order base scheme.

The approach is prompted partly by a need for an efficient method which is capable of highly resolved DNS of compressible turbulence in the presence of shock waves for a variety of flow speeds and partly by the need for the preservation of vortex convection and fine scale flow structure capturing. The five test cases illustrate the versatility of the proposed schemes in accurately capturing a variety of flow features, where most conventional methods exhibit difficulty in obtaining low-dissipative solutions in an efficient and stable manner. Higher accuracy is achieved with fewer grid points when compared with standard TVD or ENO schemes. In all of the test cases, if adaptive grid refinements were used, additional gain in efficiency and accuracy should be realized. Application of these schemes for time marching to the steady states is a subject of future research.

ACKNOWLEDGMENTS

REFERENCES

1. J. C. Hardin, J. R. Ristorcelli, and C. K. W. Tam, Eds., *Workshop on Benchmark Problems in Computational Aeroacoustic*, NASA Conference Publication 3300 (1995).

2. N. D. Sandham and H. C. Yee, *Performance of Low Dissipative High Order TVD Schemes for Shock–Turbulence Interactions*, RIACS Technical Report 98.10 (NASA Ames Research Center, 1998).

3. E. F. Toro, Viscous flux limiters, in *Proceedings of the 9th GAMM-Conference on Numerical Methods in Fluid Mechanics*, edited by J .B. Vos, A. Rizzi, and I. L. Ryhming, Notes on Numerical Fluid Mechanics (1991), Vol. 35, p. 592.

4. B. Gustafsson and O. Olsson, Fourth-order difference method for hyperbolic IBVPs, *J. Compnt. Phys.* **1177**, 300 (1995).

5. A. Harten, The artificial compression method for computation of shocks and contact discontinuities. III. Self-adjusting hybrid schemes, *Math. Comp.* **32**, 363 (1978).

6. A. Harten, A high resolution scheme for computation of weak solutions of hyperbolic conservation laws, *J. Comput. Phys.* **49**, 35 (1983).

7. A. Harten, On a class of high resolution total-variation-stable finite-difference schemes, *SIAM J. Numer. Anal.* **21**, 1 (1984).

8. H. C. Yee, On symmetric and upwind TVD schemes, in *Proceedings of the 6th GAMM-Conference on Numerical Methods in Fluid Mechanics, Sept. 1985, Gottingen, Germany.*

9. H. C. Yee, Construction of explicit and implicit symmetric TVD schemes and their applications, *J. Comput. Phys.* **68**, 151 (1987); also NASA TM-86775, July 1985.

10. H. C. Yee, Explicit and implicit compact high-resolution shock-capturing methods for multidimensional Euler equations. I. Formulation, NASA TM-110364, Aug. 1995; also *J. Comput. Phys.* **131**, 216 (1995).

11. C. W Gear, *Numerical Initial Value Problems in Ordinary Differential Equations* (Prentice Hall, Englewood Cliffs, NJ, 1971).

12. J. D. Lambert, *Computational Methods in Ordinary Differential Equations* (Wiley, New York, 1973).

13. J. C. Butcher, *Numerical Analysis of Ordinary Differential Equations* (Wiley, Chichester, 1987).

14. M. Carpenter and C. A. Kennedy, Fourth-order 2N storage Runge–Kutta schemes, NASA TM-109112, June 1994.

15. S. Gottlieb and C.-W. Shu, *Total Variation Diminishing Runge–Kutta Schemes*, ICASE Report No. 96-50 (1996).

16. S.-W. Shu, Efficient implementation of essentially non-oscillatory shock-capturing schemes, II, *J. Comput. Phys.* **83**, 32 (1989).

17. R. S. Hirsh, Higher order accurate difference solutions of fluid mechanics problems by a compact differencing technique, *J. Comput. Phys.* **19**, 90 (1975).

18. M. Ciment and H. Leventhal, Higher order compact implicit schemes for the wave equation, *Math. Comp.* **29**, 985 (1975).

19. S. Lele, Compact finite difference schemes with spectral-like resolution, *J. Comput. Phys.* **103**, 16 (1992).

20. R. Hixon and E. Turkel, High-accuracy compact MacCormack-type schemes for computational aeroacoustics, AIAA Paper 98-0365, 36th Aerospace Sciences Meeting & Exhibit, Reno, NV, Jan. 12–15, 1998.

21. D. Gottlieb and E. Turkel, Dissipative two–four methods for time dependent problems, *Math. Comp.* **30**, 703 (1976).

22. A. Bayliss, P. Parikh, L. Maestrello, and E. Turkel, *A Fourth-Order Scheme for the Unsteady Compressible Navier Stokes Equations*, ICASE Report No. 85-44 (1985).

23. G. Strang, On the construction and comparison of difference schemes, *SIAM J. Numer. Anal.* **5**, 506 (1968).

24. M. Gerritsen, *Designing an Efficient Solution Strategy for Fluid Flows*, Ph.D. thesis, SCCM Program, Stanford University, Oct. 1996.

25. P. Olsson, Summation by parts, projections and stability, *Math. Comp.* **64**, 1035 (1995).

26. P. Olsson, Summation by parts, projections and stability, II, *Math. Comp.* **64**, 212 (1995).

27. A. Harten, *On the Symmetric Form of Systems for Conservation Laws with Entropy*, ICASE Report 81-34, NASA Langley Research Center (1981).

28. H.-O. Kreiss and Scherer, *On the Existence of Energy Estimates for Difference Approximations for Hyperbolic Systems*, Technical Report, Department of Scientific Computing, Uppsala University (1977).

29. B. Strand, Summation by parts for finite difference approximations for d/dx, *J. Comput. Phys.* **110**, 47 (1994).

30. H. C. Yee, Linearized form of implicit TVD schemes for multidimensional Euler and Navier–Stokes equations, *Comput. Math. Appl.* **12A**, 413 (1986).

31. H. C. Yee, A class of high-resolution explicit and implicit shock-capturing methods, VKI Lecture Series 1989-04 Mar. 6–10, 1989; also NASA TM-101088, Feb. 1989.

32. H. C. Yee, G. H. Klopfer, and J.-L. Montagne, High-resolution shock-capturing schemes for inviscid and viscous hypersonic flows, *J. Comput. Phys.* **88**, 31 (1990).

33. B. Engquist and B. Sjogreen, High order shock capturing methods, in *CFD Reviews*, edited by Hafez and Oshima (Wiley, New York, 1995), pp. 210–233.

34. R. Donat, Studies on error propagation for certain nonlinear approximations to hyperbolic equations: Discontinuities in derivatives, *SIAM J. Numer. Anal.* **31**, 655 (1994).

35. M. Carpenter and J. H. Casper, The accuracy of shock-capturing in two spatial dimensions, AIAA-97-2107, in *Proceedings of the 13th AIAA CFD Conference, Snowmass, CO, 1997*, p. 488.

36. A. Jameson, W. Schmidt, and E. Turkel, Numerical solutions of the Euler equations by finite volume methods using Runge–Kutta time-stepping schemes, AIAA Paper No. 81-1259, 1981.

37. H. C. Yee and A. Harten, Implicit TVD schemes for hyperbolic conservation laws in curvilinear coordinates, AIAA Paper 85-1513, in *Proceedings of the AIAA 7th CFD Conference, Cincinnati, Ohio, July, 1985*; also *AIAA J.* **25**, 266 (1987).

38. P. L. Roe, *Some Contributions to the Modelling of Discontinuous Flows*, Lectures in Applied Mathematics, Vol. 22 (Amer. Math. Soc., Providence, RI, 1985).

39. P. L. Roe, Approximate Riemann solvers, parameter vectors, and difference schemes, *J. Comput. Phys.* **43**, 357 (1981).

40. A. Harten and J. M. Hyman, A self-adjusting grid for the computation of weak solutions of hyperbolic conservation laws, *J. Comput. Phys.* **50**, 235 (1983).

41. S. Jin and J.-G. Liu, The effects of numerical viscosities. I. The slowly moving shocks, *J. Comput. Phys.* **126**, 373 (1996).

42. H. C. Yee and J. Shinn, Semi-implicit and fully implicit shock-capturing methods for hyperbolic conserva-
tion laws with stiff source terms, AIAA-87-1116, in *AIAA 8th CFD Conference, June 1987, Hawaii*; also,
AIAA J. **27**, 299 (1989).

43. V. Y. C. Young and H. C. Yee, Numerical simulation of shock wave diffraction by TVD schemes, AIAA Paper
87-0112, 1987.

44. R. M. Beam and R. F. Warming, An implicit finite-difference algorithm for hyperbolic systems in conservation
law form, *J. Comput. Phys.* **22**, 87 (1976).

45. F. Davoudzadeh, H. McDonald, and B. E. Thompson, Accuracy evaluation of unsteady CFD numerical
schemes by vortex preservation, *Comput. Fluids* **24**, 883 (1995).

46. N. D. Sandham and W. C. Reynolds, *A Numerical Investigation of the Compressible Mixing Layer*, Report
TF-45, Department of Mechanical Engineering, Stanford University (1989).

47. T. Lumpp, Compressible mixing layer computations with high-order ENO schemes, in *15th Intl. Conf. on
Num. Meth. in Fluid Dynamics, Monterey, June 1996.*

48. D. Fu and Y. Ma, A high order accurate difference scheme for complex flow fields, *J. Comput. Phys.* **134**, 1
(1997).

49. N. D. Sandham and H. C. Yee, A numerical study of a class of TVD schemes for compressible mixing layers,
NASA TM-102194, May 1989.

50. S.-W. Shu, G. Erlebacher, T. A. Zang, D. Whitaker, and S. Osher, *High-Order ENO Schemes Applied to Two-
and Three-Dimensional Compress Flow*, ICASE Report 187562, NASA Langley Research Center (1991).

51. H. C. Yee, N. D. Sandham, and M. J. Djomehri, *Low Dissipative High Order Shock-Capturing Methods Using
Characteristic-Based Filters*, RIACS Technical Report 98.11 (May 1998).

52. G. N. Coleman, J. Kim, and R. D. Moser, A numerical study of turbulent supersonic isothermal-wall channel
flow, *J. Fluid Mech.* **305**, 159 (1995).

53. J. Kim, P. Moin, and R. D. Moser, Turbulence statistics in fully developed turbulent channel flow at low
Reynolds number, *J. Fluid Mech.* **177**, 133 (1987).

54. N. D. Sandham and R. J. A. Howard, Direct simulation of turbulence using massively parallel computers,
Parallel Computational Fluid Dynamics '97, edited by D. R. Emerson *et al.* (Elsevier, Amsterdam/New York),
23 (1998).